University of South Carolina
Scholar Commons

Theses and Dissertations

2016

Mechanical Characterization of SICF-SICM Nuclear Fuel Cladding by a Novel Hydraulic Internal Pressurization Method

Kirill Shapovalov
University of South Carolina

Follow this and additional works at: http://scholarcommons.sc.edu/etd

 Part of the Mechanical Engineering Commons

Recommended Citation

Shapovalov, K.(2016). *Mechanical Characterization of SICF-SICM Nuclear Fuel Cladding by a Novel Hydraulic Internal Pressurization Method.* (Master's thesis). Retrieved from http://scholarcommons.sc.edu/etd/3567

This Open Access Thesis is brought to you for free and open access by Scholar Commons. It has been accepted for inclusion in Theses and Dissertations by an authorized administrator of Scholar Commons. For more information, please contact SCHOLARC@mailbox.sc.edu.

MECHANICAL CHARACTERIZATION OF SiC_F-SiC_M NUCLEAR FUEL CLADDING BY A NOVEL HYDRAULIC INTERNAL PRESSURIZATION METHOD

by

Kirill Shapovalov

Bachelor of Science
University of South Carolina, 2014

Submitted in Partial Fulfillment of the Requirements

For the Degree of Master of Science in

Mechanical Engineering

College of Engineering and Computing

University of South Carolina

2016

Accepted by:

Xinyu Huang, Director of Thesis

George Jacobsen, Reader

Lacy Ford, Senior Vice Provost and Dean of Graduate Studies

© Copyright by Kirill Shapovalov, 2016
All Rights Reserved.

DEDICATION

This work is dedicated to the people who devote their lives and work to the common good for the humanity, to the science and technology industries and those who support education and creativity in other people. This work is dedicated to those who move our society to a brighter future.

ACKNOWLEDGEMENTS

I would like to express my appreciation to Dr. Xinyu Huang, who provided me with the opportunity to conduct this research and for all the mentoring along the way. I am thankful to Dr. George Jacobsen for the valuable feedback on the research progress. I would like to show my appreciation to my family and friends who supported me during times when it mattered most and for all the joyful times in between.

This work was performed at the University of South Carolina, Mechanical Engineering Department, in collaboration with General Atomics. Funding was provided by the Department of Energy Office of Nuclear Energy under the Accident Tolerant Fuel Program, DE-NE0000566 and DE-NE0008222. This report was prepared as an account of work partially sponsored by an agency of the United States Government. Neither the United States Government nor any agency thereof nor any of their employees make any warranty, express or implied, or assumes any legal liability or responsibility for the accuracy, completeness, or usefulness of any information, apparatus, product, or process disclosed, or represents that its use would not infringe privately owned rights. Reference herein to any specific commercial product, process, or service by trade name, trade mark, manufacturer, or otherwise does not constitute or imply its endorsement, recommendation, or favoring by the United States Government or any agency thereof. The views and opinions of the authors expressed herein do not necessarily state or reflect those of the United States Government or any agency thereof.

ABSTRACT

Ceramic Matrix Composites (CMC) have been actively researched for applications requiring high temperature strength and damage tolerance. Examples are turbine engine hot section components, leading edges for hypersonic vehicles, nuclear fusion reactor first wall and blanket, and recently nuclear fuel claddings. Predictable material damage behavior is desirable for these applications so early damage accumulation can be detected before a catastrophic failure occurs. Many ceramic materials can withstand high temperature environments, but due to inherent brittleness of ceramics the high damage tolerance and the predictable damage behavior are difficult to achieve. Ceramic fiber reinforced ceramic composites (CFCC) have demonstrated the above properties through properly designed fiber architecture, carefully engineered fiber-matrix interphase layer, and the advanced manufacturing processes. Because of the number of unknowns associated with the design and manufacturing of CFCCs, mechanical experiments are relied upon to obtain necessary material property data sets for component and system design analysis.

This work focuses on: (1) development and validation of novel mechanical characterization techniques for tubular samples; and (2) characterization of a nuclear grade silicon carbide fiber reinforced silicon carbide matrix (SiC_f-SiC_m) composite nuclear fuel cladding. A bladder type internal pressure fixture was designed to load the composite cladding tubes to failure in two configurations: tubular sample with both ends

open and tubular sample with one closed-end. The test methods were first validated by testing tubular surrogate samples made out of well-known materials, and comparing the test results with finite element (FE) simulation and analytical calculations. The pressure profile measured by Digital Image Correlation (DIC) along sample axis is in good correlation with previously reported analytical solution. Away from the edge, the measured strains were found to be within 3% of calculated values at loading levels of interest. A closed-end validation experiments showed that the novel bladder method can generate a hydrostatic pressure state which closely imitates the operating conditions for nuclear fuel claddings.

Using the above methods, nuclear grade SiC_f-SiC_m composite tubes had been tested in both configurations to obtain critical stress and strain values at proportional limit and at failure. One group of samples, with only 1.25 mm wall thickness, was able to sustain internal pressures averaging at 99.8 MPa before the final rupture. These samples also demonstrated pronounced progressive damage behavior starting around 33.2 MPa. At the rupture pressure, all samples showed graceful failure modes without excess fragmentation. The surface strain maps measured by DIC revealed highly heterogeneous strain state during loading; the spatial frequency of the strain patterns correlate to the fiber tow braiding architecture. At final failure, the local peak strain was found to range between 115% and 185% of the average failure strain observed on sample surfaces.

Acoustic emission (AE) monitoring method was used to obtain additional information about the progressive damage behavior in this CFCC. From activity and intensity of the captured AE signals, a strong correlation had been observed when stress approaches proportional limit, the first significant damage state in CMC. Contrary to the

commonly observed Kaiser and Felicity effects, an interesting new phenomenon of AE signal bursts during unloading process was observed for some SiC_f-SiC_m composite tubes. It is hypothesized that it is related to the forced closure of mismatched crack surfaces. Frequency content of some AE signals was shown to decrease with the increased amount of damage. Unsupervised Pattern Recognition (UPR) technique was applied to identify and group similar AE signals. Four classes were identified with the clustering algorithms showing consistency with other works. It is believed that the classes are associated with microscopic composite damage mechanisms such as matrix cracking, fiber breaking, fiber-matrix debonding and sliding. Such correlation, with further verification, will help elucidate the progressive damage process of CMCs.

TABLE OF CONTENTS

LIST OF FIGURES

LIST OF ABBREVIATIONS

AE ..... Acoustic Emission

AOI ..... Area of Interest

CFCC .....Ceramic Fiber Ceramic Composite

CMC.....Ceramic Matrix Composite

CVI.....Chemical Vapor Infiltration

DIC..... Digital Image Correlation

EPD..... Electrophoretic Deposition

FE.....Finite Element

HDT .....Hit Definition Time

HLT.....Hit Lockout Time

ID .....Inside Diameter

LWR.....Light Water Reactor

NITE ..... Nano-Infiltration and Transient Eutectic

OD..... Outside Diameter

PCMI.....Pellet Cladding Mechanical Interaction

PDT.....Peak Definition Time

PLS..... Proportional Limit Stress/Strength

SiC.....Silicon Carbide

SPR .....Supervised Pattern Recognition

UPR.....Unsupervised Pattern Recognition

UTS.....Ultimate Tensile Stress/Strength

CHAPTER 1. INTRODUCTION

1.1 Motivation and Background

Silicon carbide fiber reinforced silicon carbide matrix (SiC_f-SiC_m) composites are being actively pursued by a scientific community for an accident tolerant nuclear fuels cladding applications. The SiC_f-SiC_m composite cladding have being considered as a replacement for a zirconium cladding tube and it has shown to have many desirable attributes including high strength at high temperatures, stability under irradiation, low reactivity with the hot coolant, and low hydrogen production [1-3]. However, while the material itself has the desired properties, the nature of the ceramic composites makes designing it to be a challenging problem. The fiber architecture, interphase deposition and manufacturing processes are difficult to predict accurately, therefore composite characterization still heavily relies on material testing.

Two examples of highly important mechanical tests are the internal pressure burst test and the end plug push out test. Both tests evaluate the composite strength in a LOCA (loss-of-coolant accident) scenario when the internal pressure of the cladding rises beyond normal operating conditions. The end plug test evaluates a joint strength between the cladding tube and the plug as it also must withstand the high pressures causing high push out forces on the plug. Many tests were developed for measuring hoop stresses/strains during a burst pressure test [4-7]. Elastomeric insert method of such testing has being already standardized. A method for testing plug joints in its final

geometrical shape had recently being submitted to ASTM but there still exists a lack of proven methods [1, 2]. In this work, an alternative method was developed for pressure testing silicon carbide nuclear grade composites in both tubular and closed-end configurations using a novel polymer bladder apparatus.

The potentials of Ceramic Matrix Composites (CMC) as a structural material in high temperature applications had been first recognized in mid-1970s and it has been actively studied for several decades [8]. The main advantages that these composites offer over metal parts are the ability to retain strength under continuously high operating temperatures and a weight reduction of the components. In turbine engines these advantages provides higher engine efficiency which translates to fuel savings. In addition, ceramic composites provide much improved toughness and damage tolerance over the equivalent monolithic materials. The key to improved toughness is a properly engineered fiber matrix interphase. By depositing a weak interphase material on the fiber surface with a relatively low shear modulus, a matrix crack tip can be diverted away from the load carrying fibers as shown in Figure 1.1 [9]. Another significant challenge associated specifically with non-oxide composites was to prevent oxidation. When the fibers are exposed to oxidizing environments, the composites can lose their toughness due to interphase degradation. However, a novel self-healing interphase and matrix structures had been designed [8], once again qualifying these materials for high temperatures and oxidizing environments such as turbine engines and nuclear reactors.

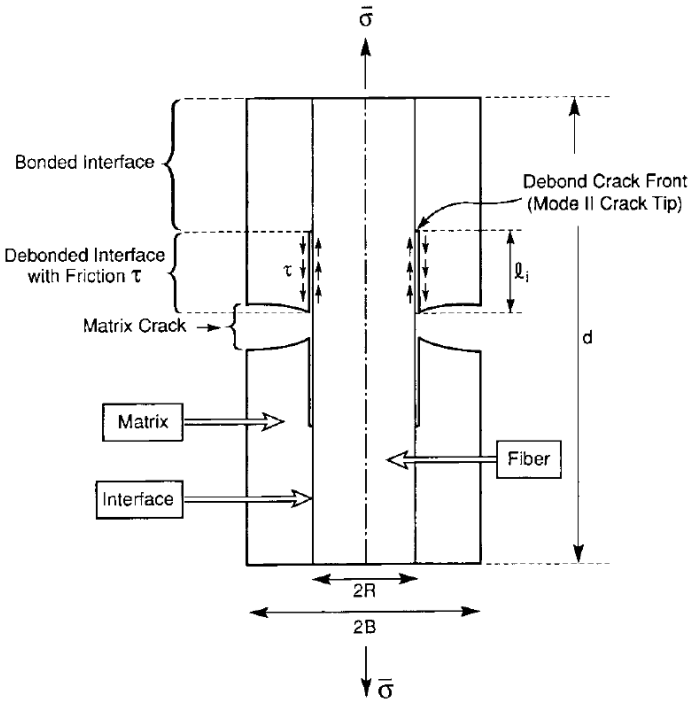

Figure 1.1 Matrix crack redirected paralell to the loading by a weak fiber-matrix bond [12].

As Naslain [8] reports, practical applications of these composites had been exploit in the stationary parts of jet engines and power generators such as combustor chamber liners and exhaust nozzles. Replacing heavy superalloy components with these ceramics had provided higher engine efficiencies, lower emissions and greater fuel economy by increasing operating temperatures, eliminating the need of cooling these parts and through a weight reduction. However, the durability, corrosion resistance and economical aspects remain to be questionable for these materials. In the nuclear industry, CFCC composites are researched for the fusion reactor first wall, blanket and divertor [8] and a cladding material for the light water reactors [10]. The operating environment would not only be high temperature and corrosive, due to coolant, but it will also be

highly radioactive with neutrons and alpha particles. The SiC_f-SiC_m composites are the most promising for such application due to its low residual radioactivity after being irradiated and a high stability under irradiation [8]. However, there are several issues that need to be addressed before an implementation stage. Under irradiation and high temperatures, some of the issues include the geometrical changes of the matrix and the fibers, instability of the interphase material after prolong exposure, lowered fiber strength, decreased thermal conductivity, especially through thickness direction, and SiC_f-SiC_m may react with the gases present in a reactor (oxygen, helium and hydrogen). Nevertheless, SiC_f-SiC_m is the most promising material choice from the CMC family.

Manufacturing of these CMC composites had evolved into several basic routes: (1) when the matrix precursor is in liquid phase, (2) in gaseous phase, (3) a slurry type, and (4) a combination route [8]. A few other methods are under development including electrophoretic deposition (EPD) [11]. Liquid phase route splits into a polymer impregnation/pyrolysis (PIP) method and a liquid silicon infiltration (LSI). PIP process works on impregnating a fiber preform with a Si-C precursor in a liquid state. The precursor flows through the fiber network wetting the fibers. However, this method produces a matrix structure with high porosity. To improve densification, several cycles of PIP process could be used. Repeating of the cycles makes it less economical and slow. To improve densification while reducing the number of impregnation cycles, fillers, such as fine powder of silicon carbide, can be added to the precursor. Yet, fillers make it more difficult to impregnate the preform. The other method, liquid silicon infiltration, often referred as LSI, starts by depositing carbon with PIP or a chemical vapor infiltration (CVI) process to a porous preform. The preform is then filled with liquid silicon or a

silicon based alloy which occupies the remaining pores providing a highly dense composite. However, the process is performed at high enough temperatures (1400°C - 1600°C) when some types of fibers can be weakened. Liquid silicon is also corrosive to fibers and to some interface materials unless a specially prepared hex-BN/SiC interphase is used. Lastly, additional treatments must be performed in order to reduce an amount of free silicon which lowers creep resistance.

Matrix, interphase and additional coatings can also be deposited onto a preform in a gaseous state, which is the second approach called chemical vapor infiltration (CVI) [8]. This method could be done at lower temperatures, compared to the liquid phase approach, and at low or atmospheric pressures. The fiber preform must contain and maintain a pore network for the gases to flow until the densification process is completed. Several variations of the method had evolved in order to maintain the pore channels opened and to increase the speed of infiltration. These variation including isothermal/isobaric process (I-CVI), pressure gradient (PG-CVI), inverse temperature gradient (TG-CVI), combination of the pressure gradient and inverse temperature gradient techniques called forced (F-CVI) and a pressure-pulse process (P-CVI). The CVI approach offers a high degree of control of the composite microstructure. The main drawback to CVI method, regardless of the process variation, is the significant residual porosity which can cause lower strengths and thermal conductivity.

The third process route, slurry method, had been disregarded for some time because the process was excessively detrimental to the fibers. However, recent improvements had brought it back. In this method, fibers are passed through a slurry bath that contains silicon carbide powder and then the fibers are wounded onto a drum [8].

The composite is then sintered at high temperature and pressures. Previously, it is this step that caused damage to the fibers. However, it was discovered that adding sintering agents, especially oxide type, permits lower temperatures. When thermally stable quasi-stoichiometric fibers are combined with these oxide type additives, the process yields composites with low porosity, high mechanical properties and high thermal conductivity. This process is known as NITE, nano-infiltration and transient eutectic phase. However, the fiber volume fraction remains small and the interphase layer is still relatively thick.

Composites go through several damage mechanisms when loaded in tension. Significant contributions in understanding CMC failure behavior were made by Veggagini and Evans. A typical stress-strain curve for a non-oxide CMC is shown in Figure 1.2 [9]. When a composite is loaded, it goes through three main damage states. During initial loading, the material behaves elastically as no significant damage had occurred yet. Once the stress reaches the matrix crack stress, $\overline{\sigma_{mc}}$, or a Proportional Limit Stress (PLS), the material starts to accumulate irreversible damage in a form of matrix cracking, fiber breaking, and fiber-matrix debonding. Further loading increases the matrix crack density up to a saturation state, $\overline{\sigma_s}$. After this point, any additional increase in stress is carried by the fibers only. Some composites, however, fail before reaching matrix crack saturation. Particularly, Veggagini studied hysteresis loops and some of the damage mechanisms during loading-unloading cycles between the PLS and the crack saturation states. The amount of hysteresis provides information on the fiber-matrix interface bond. Larger hysteresis loop width indicates smaller debond energy between the fiber and the matrix. This condition is also accompanied by a quadratic path of the unloading curve all the way to zero stress. When the material has a large debond

energy, as identified by Vagaggini, the hysteresis loop has a narrower loop width and a linear portion right before unloading to zero stress. A hysteresis loop is observed in combination with the permanent strain when fully unloaded. This strain includes the contributions from the misfit strain and the matrix crack opening produced during the fiber-matrix debonding, Figure 1.2. This analysis brings better understanding of the constituent properties of the CMC composites and aids in interpreting test results.

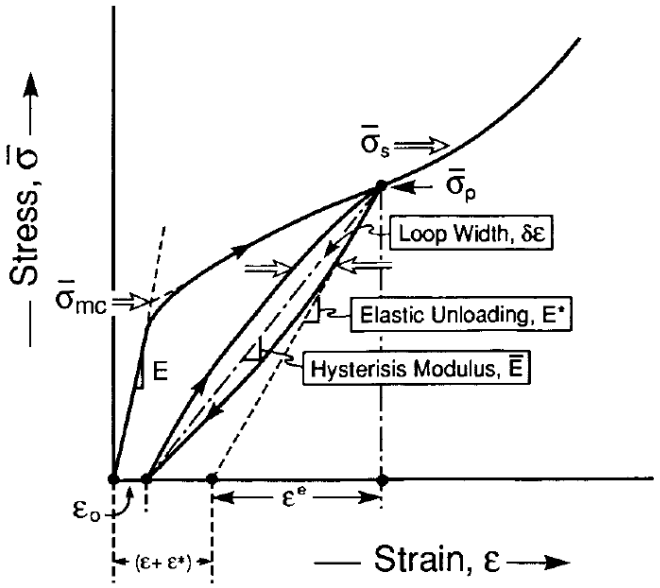

Figure 1.2 Typical stress-strain curve for CMC during cycling loading [12].

1.2 Open-end Burst Testing

An internal pressure burst test is a common test method for tubular structures that need to sustain high internal pressures during operations, such as nuclear fuel cladding. Various test methods had been developed to pressure load tubular specimens. Mosley [12] used an elastomer insert method, also known as a polymer plug test, where a cylindrical elastomer is compressed inside a sample. An axial compression causes the

polymer insert to expand in a radial direction, therefore inducing pressure on the inner walls of a sample. It was noticed that the elastomer insert behaves like a hydraulic fluid up to 5% of axial compression. Through an analytical solution, stress profiles on the inside and the outside walls were derived. These stress profiles were compared to experimental results of mild steel tubes and matched within 5%. Mosley also showed that applying lubricant between the insert and the sample, between the insert and the actuating rods reduces friction and hence brings the experimental results closer to the theoretical values. The insert material has to be carefully chosen since some elastomers might be difficult to machine to a desired outside diameter and they can be dimensionally unstable under cycling loadings. Nevertheless, the method is relatively simple to implement on traditional mechanical testing machines, requires little time to set up and does not require a mechanical bonding to the test samples. These advantages make it a popular choice for an internal pressure generation and it has evolved into an ASTM C1819-15 [13] standard. Byun [5] had utilized the plug test to show size effects in miniature alumina tubes. Ross [14] had compared experimental results from monolithic and composite ceramic tubes using the polymer insert method. It is worth to note, however, that buckling of these polymer plugs can occur when the ratio of length over diameter of the plug gets large. This factor limits the length of a sample that can be tested with this method.

A segmented cone method had been proposed by Nilsson [15] to produce radial forces onto a cylindrical sample by pushing in a cone through matching contact surface segments. The method provides a good control of radial displacement and is relatively easy to set up. On the other hand, some of the friction coefficients between the segments

and a sample are hard to control. Also, mechanical contact pressure is not continuously distributed on the internal surface of the samples, consequently introducing undesired stress concentration at segments edges.

Another way of generating internal pressure is by pressurizing liquid inside of a tubular sample. This method often times required some sort of seal between an experimental fixture and a test specimen. In works reported by Cain [16] and Cohen [17], two similar fixtures were developed to test composite samples using pressurized oil. Two parallel plates were spaced just far enough for a test sample to fit in between. A soft material was placed on the inside wall of the sample to act as an oil seal. When the oil is pressurized, the seal pressed against a specimen inducing stresses in a radial direction. A small amount of pressure was lost due to seal compression. Both authors reported that their methods produced a uniform pressure on the samples. Brown [18] utilized a similar fixture setup for testing bone specimens, but instead of oil an inert nitrogen gas was used. For most applications though, gas should be avoided as a pressurized medium due to a significantly higher danger levels associated with a rapid gas release when a specimen fails. It is worth noting that in all of these tests the sample edges were loaded to the same pressure as the rest of the material creating a significant edge effect.

1.3 Closed-end Burst Testing

Light Water Reactor (LRW) nuclear fuel cladding is a fully sealed tube, typically through a use of end plug seals. Creating a strong bond between the end plug and the SiC_f-SiC_m tube that is stable under reactor core conditions has only recently been demonstrated [10]. It is desirable to evaluate the strength of the joined tubes under pressures encountered in real service condition. For planar geometries, a good number of

test methods had been developed to measure shear strength of ceramic composite joints such as four point bend, single lap offset shear, double-notched shear, torsion shear and etc. [10, 19-21]. However, Khalifa and Katoh [1, 10] had stressed out the need to develop a more representative test method where structural geometries are included in joint strength testing. Khalifa had evaluated silicon carbide monolithic and composite tubes with end plugs using a newly developed push out test. A push rod was used to pass through the tubular part of the sample and to push the plug out. Samples were supported by a bonded conical shape collet resting on a rigid structure of the fixture. Custom made parts can be easily integrated with a standard mechanical testing machine which makes it a convenient testing method. The author demonstrated that the more traditional planar flexural testing for joint strength alone is not enough to predict structure strength of a more complicated geometrical shape. Khalifa had successfully compared several different end plug/sample bonding configurations.

At the moment of writing, no other work testing a composite material with a geometry similar to cladding end plug is known to the author. As reported by Katoh [10], there exists a lack of testing methods capable of producing more relevant loading conditions for a pressurized tube with an end plug. For that reason a novel method was developed using a common hydrostatic bladder method but for tubular samples with an end plug. The hydrostatic pressurization method is believed to be more stress state representative than traditional planer shear strength test methods.

1.4 Mechanical Characterization of Nuclear Grade SiC_f-SiC_m Composites

In the last two decades a great amount of research effort was directed towards the characterization of nuclear grade SiC_f-SiC_m composites [1-4, 7, 22, 23]. Nozawa et al.

had tested unidirectional composites produced by NITE method and plain-wave composites produce by CVI and NITE methods in tension, compression and shear with ranging fiber angles [22]. Resulting properties at PLS and at final fracture were reported. The results showed that CVI composites have a significantly greater tensile and shear strengths than the other two composites with the same fiber angles. Nozawa also pointed out that the failure stresses could be predicted with the Tsai-Wu criterion fairly accurately. Rohmer et al. had performed axial and hoop loading tests at ambient temperatures on braided SiC_f-SiC_m cladding produced by CVI method [4]. Mechanical properties obtained by Rohmer were significantly lower than the ones obtained by Nozawa, however, the fiber type and sample geometries were different these works. A 3D simulation model for an axial test of the composite had revealed stress concentration points where the fiber tows overlap each other. While the composites were braided and do not have laminate layers, it was reported that the delamination can happen through a fiber tow. Rohmer also suggested that because of the stress concentration produced by the contacting tows of fiber, those locations could be the initiation cites for the delamination cracks. Jacobsen et al. had investigated application of C-ring test on nuclear grade claddings [7]. By cutting a slot out from a ring and compressing the resulting C shaped samples, material mechanical properties from hoop stresses were measured and compared to results obtained from the expending plug method. Khalifa, as mentioned above, had tested SiC_f-SiC_m composites in an end plug configuration evaluating joint strength between the plugs and the tubular sections of the samples [1].

1.5 Digital Image Correlation on CMC

Digital Image Correlation (DIC) is a powerful strain measurement technique. It is a non-contact full-field strain measurement method with a broad range of applications [24]. Three-dimensional DIC method enabled by two or more cameras has been widely used to capture strain distributions on curved surfaces. A speckle pattern is first applied onto a specimen. Image sets acquired during loading are analyzed by a stereo projection and image correlation algorithms that provide displacement and strain maps on the sample surface.

This systems have been shown to be a useful tool in characterizing CMC's and SiC_f-SiC_m claddings in particular [4, 25]. The main advantage DIC has over strain gauges and extensometers is the strain field measurement type which is important for nonhomogeneous brittle materials. Rajan et al. tested 2D woven SiC_f-SiC_m dog-bone specimens loaded in tension [25]. The author used displacement fields to accurately detect matrix cracks and estimate crack opening displacement. Stress concentration regions were located where fiber tows overlapped one another. At higher stress levels, those stress concentration regions served as crack initiation sites. Rohmer et al. used DIC for strain measurement and crack density estimation [4]. The author pointed out that while DIC and strain gauges provided similar results, DIC could provide strain measurements in both hoop and axial directions for the same location. Also, during axial testing, DIC allowed to estimate the matrix crack density as a function of applied load.

1.6 Acoustic Emission Monitoring of SiC_f-SiC_m

Acoustic emission (AE) method has been gaining popularity in the scientific community expending its application range rapidly. One such area is damage characterization and early crack detection in ceramic matrix composites [3, 26-29].

AE sensors can pick up elastic waves generated by damage events in a specimen and convert it into an electrical signal, as a waveform, shown in Figure 1.3 [30]. Terms such as AE signal, AE event, and AE hit are equivalent terms referring to one signal recorded by AE acquisition system. When AE signal is detected, its parameters are calculated and a waveform is recorded. Standard parameters of a hit include duration, counts of threshold crossings (often referred as counts), rise time, counts to peak, amplitude, absolute energy, frequency centroid, peak frequency and others not used in this document. Parameters such as rise time and counts to peak have a near linear correlation. Such correlation also exists between duration and counts, and to a lesser degree between amplitude and absolute energy. A signal amplitude threshold parameter is set before running a test to eliminate AE signals of low importance and background noise. Higher threshold values decrease a number of AE hits recorded per test. AE activity refers to a number of AE hits recorded per unit time. AE intensity refers to the amplitude or absolute energy of an AE signal. Terms clusters and classes are also equivalent and refer to a group of AE events collected by clustering algorithms.

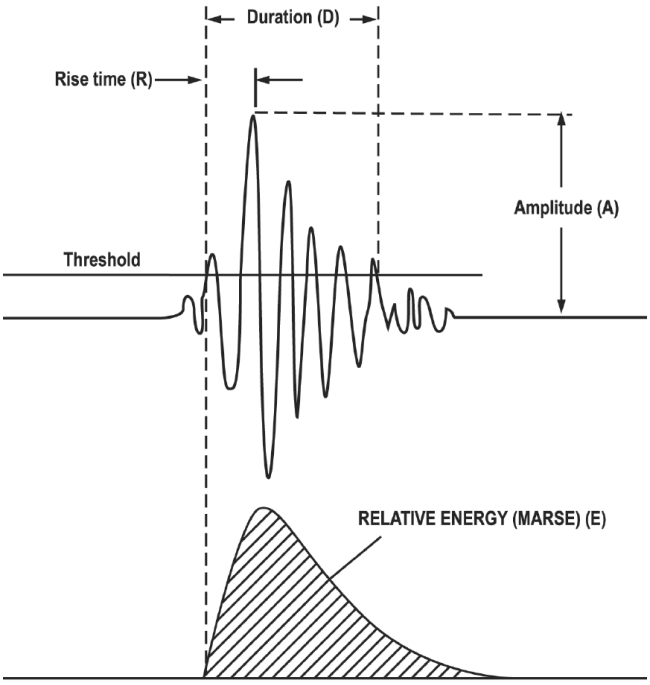

Figure 1.3 Representation of an AE signal showing major features [30].

When AE data is combined with load information, Kaiser and Felicity effects can be observed. A generic representation of such effects are found in Figure 1.4 [30]. As a material is loaded, either homogeneous or heterogeneous, from point A to point B on the graph, it continuously emits AE signals. When a specimen is unloaded, from point B to point C, the material produces no emission (AE signals from noise or an apparatus could be detected though). When the material is loaded again from point C to point B, it produces no AE signals until the previous peak load has been reached. This phenomenon is called Kaiser effect. In some cases, a deviation from Kaiser effect can be observed. For example, when the material is reloaded for the second time, from point E, AE emission starts at point F before the previous load is reached (D). This type of behavior is called Felicity effect. The exact cause of such behavior is not known [30, 31] but it is

anticipated that it has to do with unstable defects produced by substantial previous loading. Felicity ratio is a measure of the Felicity effect and is calculated by dividing the load at which the emission started during reloading by a previously reached load value. Felicity ratio had been linked to residual strength of fiber reinforced composites, but its value is dependent on the particular type of a composite [31].

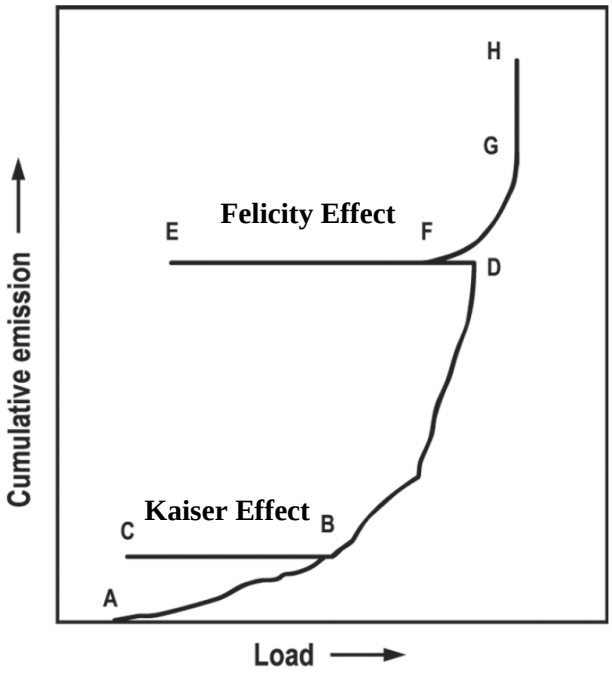

Figure 1.4 Representative graph of Kaiser and Felicity effects [30].

A typical test of a CMC can produce, depending on system setup, tens of thousands of events. Clustering algorithms can be utilized to group events with similar parameters (such as amplitude, duration, rise time etc.). These clusters can then be correlated to the physical damage mechanisms in a material. Two types of clustering algorithms are commonly used: Unsupervised Pattern Recognition (UPR) and Supervised Pattern Recognition (SPR). UPR method is used when little to no information is known

about the AE data set and the associated damage mechanisms. In this method clustering algorithms are relied upon to group similar events. SPR is used when the physical source is known about the AE events, which can be assigned to a group, for example, AE events generated by lead break tests. Then, SPR algorithms are applied to learn the characteristics of these groups. Once the SPR clustering algorithm is trained with known data, it is then used to identifying the same groups in a new AE data set. The SPR method is preferred over UPR since it offers the most predictable results, however, it is not always practical or possible to do. For composite materials, complex damage events occur simultaneously, and it is particularly difficult to generate a single type of damage mechanism for training SPR. Tests or materials can be designed to induce a specific damage mechanism (such as a fiber pull out) for generating a AE training data set. However, in a real composite, attenuation and reflections can significantly distort the AE signal [26, 32]. Because of these issues, UPR method is used in this study.

There are several widely accepted clustering algorithms available for UPR analysis. Different algorithms require different amount of user input before running an algorithm to generate the clusters. Once the clusters are obtained, assigning each cluster to a specific source is a challenging task. This is particularly the case for composite materials, which undergo multiple damage mechanisms that may occur simultaneously, such as matrix cracking, crack propagation, delamination, single fiber break, fiber bundle break, fiber pullout and friction. Some mechanisms may produce similar AE signals. Also, AE signals can be altered by the distance between the source and the sensor. Despite these challenges, AE clustering had been successfully utilized [31, 33]. Figure 1.5 shows a typical AE classification of a polymer matrix composite obtained from

Mistras training materials. It maps out AE from fiber break, matrix crack, delamination, etc., based on AE signal intensity (amplitude) and duration. Such mechanistic map is highly desired for the ceramic matrix composites as well.

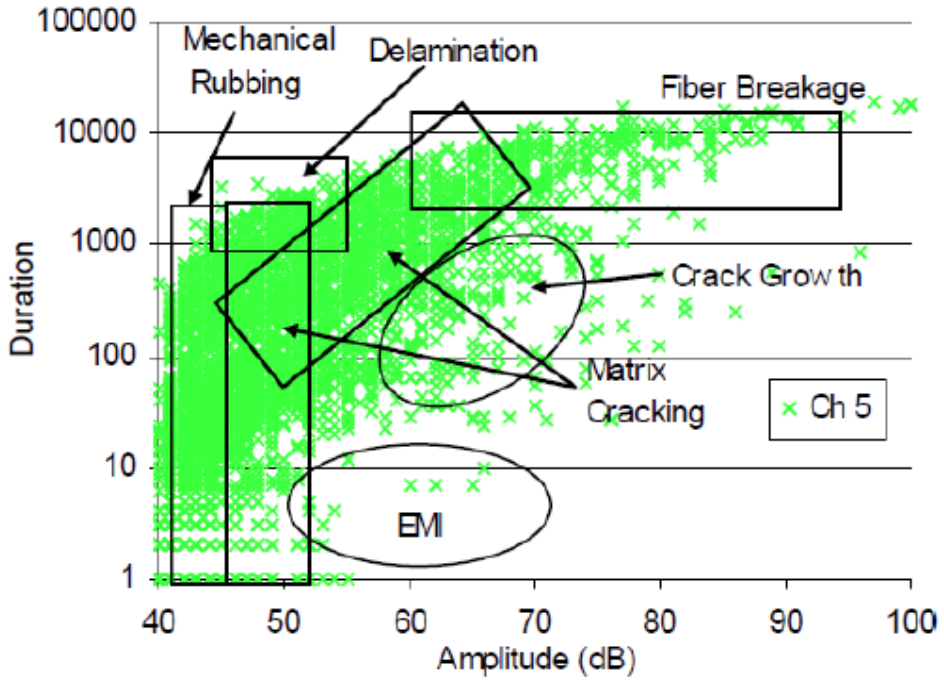

Figure 1.5 AE classification for polymer matrix composites provided by Mistras.

One of the big advantages of an AE system is the easy to incorporate AE sensor(s) to many mechanical test setups. Maillet tested SiC_f-SiC_m composites containing a single tow under tension and used UPR to analyze the AE hits [3]. After testing one of the samples and running a generic algorithm based on Davies-Buildin and Silhouette clustering performance indices, the optimum result produced only two clusters. One cluster was assigned to matrix cracking and fiber breaking and the other cluster was assigned to debonding and friction at the fiber-matrix interface. The fiber breaks and matrix cracks, while grouped to the same cluster had been differentiated based on the

strain values of the composite. Nozawa had suggested that signals with peak frequencies of around 260 kHz might be coming from matrix cracking based on tension tests [20]. Also, based on AE analysis, matrix cracking starts around 80% of PLS stress. Morscher studied AE signal attenuation and wave velocity change with increased damage state of the SiC_f-SiC_m composites [26]. It was noticed that a composite with a lower interphase shear strength shows near 85% decrease in recorded energy when the measurements are made at peak stresses.

The AE results and observations reported by other research groups serve as valuable insights which were useful during data interpretations in this work.

CHAPTER 2. EXPERIMENTAL SETUP

2.1 Open-end Burst Rig

An internal pressure burst rig was developed and first described in detail in [23], however, some further improvements have been made. The overall system setup is shown in Figure 2.1. An oil pressure is generated by a manually operated hydraulic cylinder (Model 37-6-30) from High Pressure Equipment Company. The pump is then connected to an analog pressure gauge, to aid an operator during testing. It is then connected to the burst rig. In the rig, the oil passes to a flexible polymer bladder tube (part number 5006K66 from McMaster-Carr) that deforms under oil pressure to the internal surfaces of the supporting parts and a test specimen. In this configuration, the internal pressure produces primarily hoop stresses. Axial strains are also experienced by samples due to Poisson's effect. In the original rig setup, during an assembly process, the bladder tube had to be cut longer than the supporting components (such as the sample and the adapters) to allow bladder installation. It often times caused the bladder to crumple up in the sample area which can cause non-uniform stress distribution. For that reason a telescopic adapter had been designed to be able to contract when the bladder is installed and to extend to let the bladder stretch preventing crumpling, Figure 2.2 (a). Alignment bars used in the fixture serve two functions: to center a specimen in the test rig and to eliminate axial loads being transferred to a sample. It was noticed that when a tubular sample had been cut unevenly (not perpendicular to the axis of the specimen), it caused

the whole sample-adapters assembly to “buckle” to one side which could load the sample asymmetrically. A step in the alignment bars and the mini-adapters provide a way to redirect the axial loads away for the sample to the structure of the rig, Figure 2.2 (c). Because the pressure rig consists of several components interconnected with each other, any cross-sectional change produces an axial force by the pressurized oil. The telescopic adapter has the largest cross-sectional area change such that at 70 MPa of internal pressure it would produce an axial force of nearly 4450 N which is now transmitted to the alignment bars bypassing the sample. A detailed procedure used to test samples in an open-end configuration can be found in Appendix A.

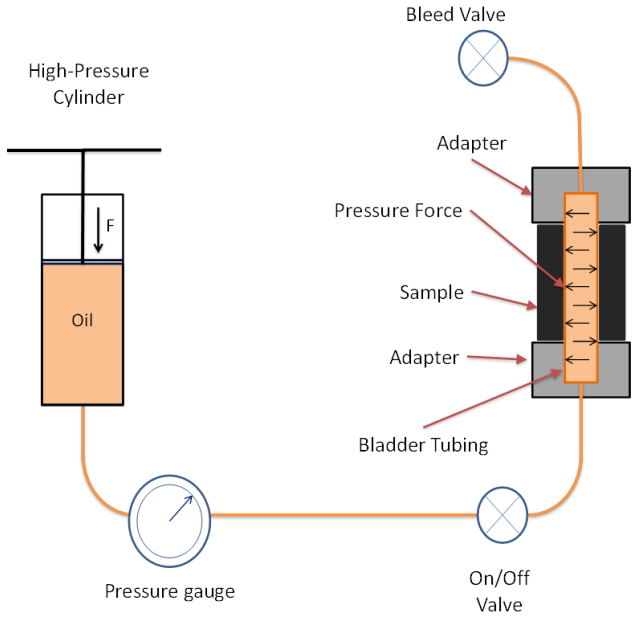

Figure 2.1 Open-end burst rig setup schematic.

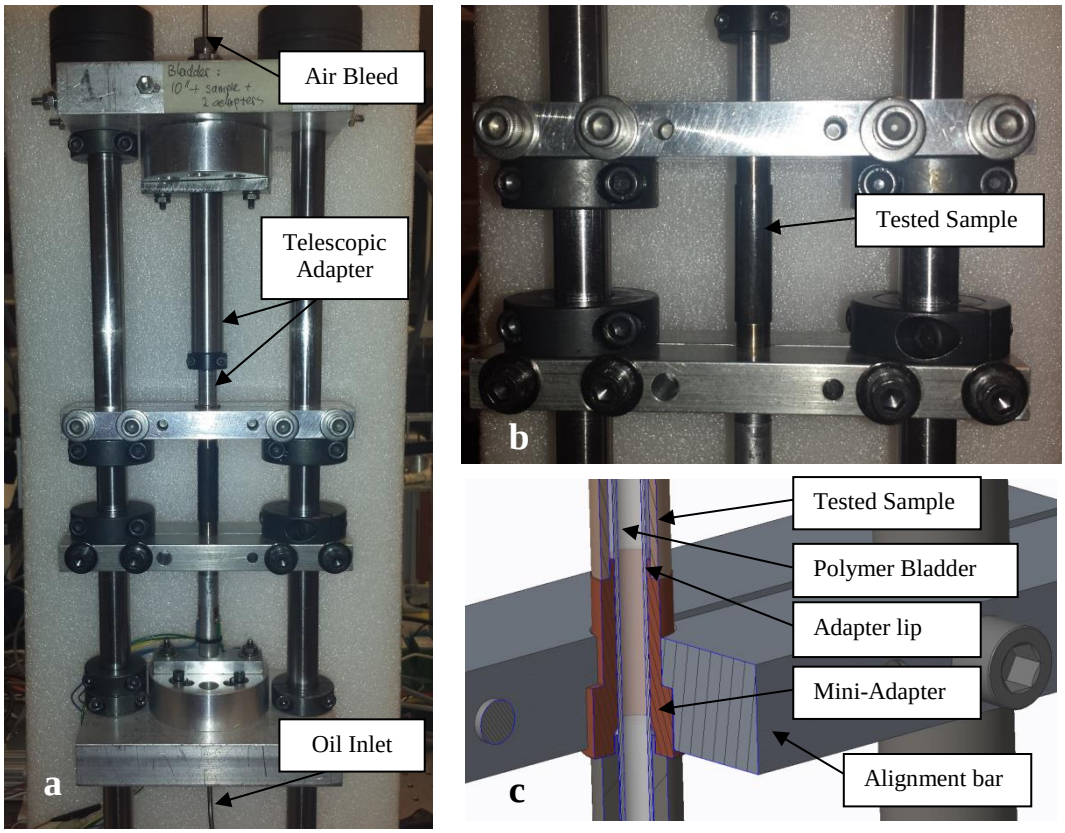

Figure 2.2 Internal pressure burst rig setup: (a) overall setup, (b) close-up of the sample, (c) computer rendering of a sample, bladder and alignment bars.

2.2 Closed-end Burst Rig

In light water reactors (LWR), the nuclear fuel cladding tubes are sealed with an end plug at both ends of the tube. A method to form a strong and a durable plug at the end of a SiC_f-SiC_m composite tube has been a challenging problem. To mechanically evaluate the strength of that connection, a novel method was developed to test SiC_f-SiC_m cladding tubes with an end plug using the internal bladder pressurization method. For the test purposes, only one end of the cladding tube is sealed with an end plug so the other end can be used to pressurize the oil inside of the tube. The general schematic of the system is shown in Figure 2.3. The closed-end burst rig is comprises of the top half of

the open-end burst rig as shown in Figure 2.4. The main difference is that the bladder tube has a polymer plug at one end produced by depositing a Liquid Stitch fabric adhesive, Figure 2.4 (c). To securely support a sample in a desired position, a metal cone is bonded to it using high shear strength epoxy, Figure 2.4 (b). Similar to the alignment bars, a sample support bar is added with a cone cutout in the middle to constrain a test sample in the axial direction. Due to an asymmetric setup, a mixed mode stress state is produced in the sample near the plug. Hoop stresses are still dominant as they are in the open-end burst rig, but the oil also produces stresses in the axial direction as shown in Figure 2.3. Because the bladder tube has only one opening, that means that the same oil line is used to fill the system up with the oil and to breed the air out. A detailed procedure used with this setup is outlined in Appendix A.

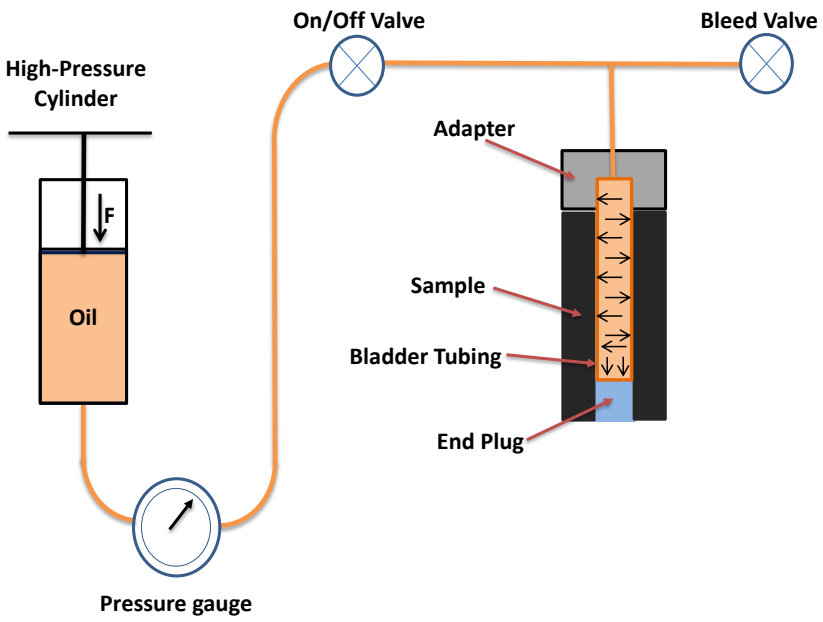

Figure 2.3 Closed-end burst rig schematic.

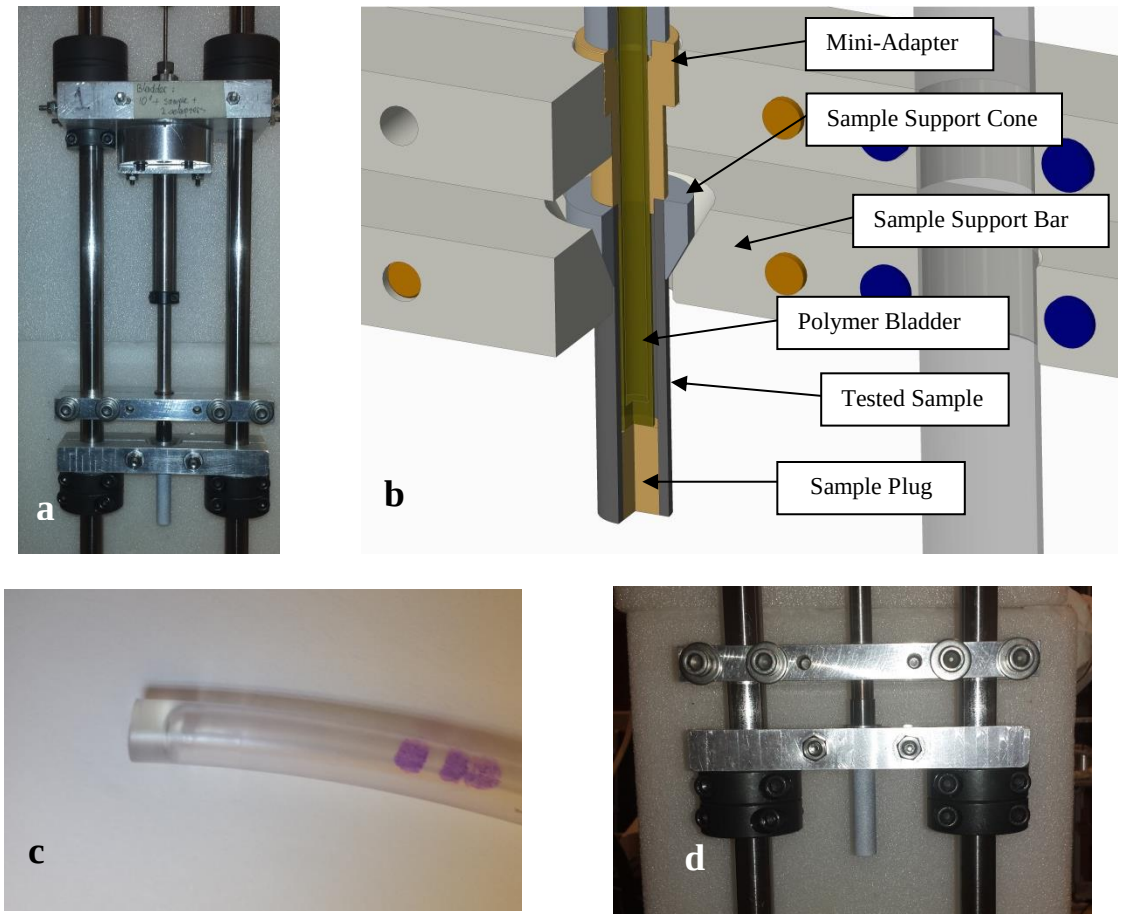

Figure 2.4 One end closed burst rig setup: (a) overall setup, (b) computer rendering of the sample connections, (c) typical bladder polymer plug, (d) close-up of the sample setup.

To make one-end closed bladder tube, two types of fabric adhesives (Liquid Stitch) were used to produce the polymer plug: a quick curing and a slow curing. The Liquid Stitch forms an elastomeric plug that bonds to the bladder tube. The slow curing type showed a significantly stronger bond to the polymer bladder therefore it was used for all of the closed-end burst tests. Once fully cured, the plug can undergo large deformations without fracturing when the bladder is pressured, and thus completely fill the inside of the closed-end sample. In order to provide a good seal against the pressurized oil, the bladder plug has to be approximately 5 mm long.

2.3 Instrumentation

During a burst test, the applied pressure, the strain state, and the acoustic emissions are monitored continuously until sample rupture. The applied hydraulic oil pressure is recorded with an Omega PX01S-20KGI pressure sensor. The sensor is connected to a National Instruments module NI 9203 which is installed in a NI c-DAQ-9172 chassis. Some tests samples are also equipped with 2 sets of CEA-06-125UT-350 strain gauges measuring strains in the axial and hoop directions. The strain gauges are connected to a NI 9237 module in the same chassis. A LabView program is written to record data from the pressure sensor and the strain gauges along with a time stamp for each record.

Digital Image Correlation system (DIC) from Correlated Solutions is used to record strain maps on the outer surface of a sample. Two monochromatic CCD type cameras (GRAS-30S5M) from Point Gray equipped with high resolution 35 mm lenses (part number 85868 from Edmund Optics) are set up with in-plain angle of about 20°. Due to such camera-lens combination and to fill the camera sensor area with an image of a sample, the cameras are placed in a close proximity of the specimen (around 150 mm away). To decrease the chance of lens damage by the burst sample fragments and oil contamination an optical glass is placed between the samples and the cameras. From simple testing, it was determined that the glass did not appear to affect DIC results. Plastic mounts originally installed on the cameras were found to be excessively flexible and they had only one screw hole for mounting to a structure. This condition would cause one camera to move and rotate independently from the other camera which consequently throws off DIC calibration. For that reason equivalent steel camera mounts

were fabricated with two mounting holes. Both cameras are rigidly mounted to a single bar which together with the new camera mounts showed a significant improvement in retaining cameras' calibration. For cylindrical samples, the two DIC cameras are oriented in the plane of sample's axis so both cameras can see the same surface. This orientation provides a strain map for approximately 90° of the sample's outer surface.

To produce a speckle pattern required for DIC measurement, the specimens are first coated with flat black paint and then sprayed with a flat white paint. The paint is sprayed manually in a way so the finer paint mist deposits on a specimen but the larger paint drops misses a specimen. The speckle pattern quality varied some due to the method but a typical speckle size was on an order of 0.05 mm across. Vic3D (by Correlated Solutions) is used for camera calibrations and to analyze captured images. During cameras calibrations, a maximum distortion order of 3 is chosen because most SiC_f-SiC_m samples have a very rough outer surface and there is a large curvature in the viewing area. A calibration target was printed and glued to a rigid thick plastic plate. Appendix B outlines the procedure used for the DIC calibration. A subset size of a computational element is automatically determined by the software. For the SiC_f-SiC_m composites, the subset step size is often times adjusted to a smaller value than recommended by the vendor of the system. This is done to decrease the amount of uncorrelated areas inside of an area of interest (AOI) that are often found on samples with rough outer surfaces. For these analyses, an optimized 8-tap interpolation option is chosen for the most accurate calculation. By default, the correlation error margin is set to 0.1 pixels and after each test the correlation error for the analyzed images is recorded. For SiC_f-SiC_m composites the correlation error is typically between 0.02 and 0.09, subset

size is between 40 and 60 pixels, step size is between 5 and 7 pixels and the strain filter is between 15 and 19 data points.

Acoustic Emission data is collected on a Micro II system from Mistras (Physical Acoustics). A resonant Nano30 sensor with a natural frequency of 300 kHz is connected to a 2/4/6 pre-amplifier which is set to 20 dB for the SiC_f-SiC_m. A petroleum based gel is used as a couplant between the AE sensor and the specimens. The sensor is enclosed in a soft polymer cover to increase its resilience to damage during sample bursts. For SiC_f-SiC_m composites, the system is set to record in a high hit rate mode which prevents it from getting oversaturated with signals. Hardware settings were determined from a pencil lead break tests (without a Neilsen Shoe) and are set at 50 PDT, 150 HDT and 350 HLT and a threshold of 55 dB. The reference gain energy is set to 20 dB by default. An analog filter boundaries are set to 100 kHz and 1 MHz. Waveform are recorded at a sampling rate of 5 million samples per second, pre-trigger of 100 μs and a signal length of 3 kilobits which corresponds to a total waveform duration of 614 μs. To reduce the number of irrelevant signals, a hit pre-filter is set to exclude signals with counts of 3 or less. For additional information on AE system setup refer to Appendix C.

2.4 Open-end Burst Rig Validation

Pressurization of a fluid is a desired way to produce hydrostatic pressure since it is the closest to imitating internal pressurization from Helium and fission gas in the nuclear fuel claddings. Pellet cladding mechanical interaction (PCMI) is not considered in this study. Sealing the oil inside of an apparatus and a sample becomes increasingly challenging with a higher number of parts in a device and with increasing maximum pressures it must sustain. A bladder tube offers a convenient way to provide a single seal

between the many components of the burst rig. The bladder tube was found to be flexible enough to largely deform inside of the apparatus. Yet, it was desired to understand whether the bladder tube produces a uniform pressure application along the sample's internal surface. For that reason validation tests had been performed.

Two photoelasticity experiments on a transparent polycarbonate surrogate sample were conducted. The sample was placed between two polarizing glass pieces illuminated by a monochromatic white light. The polarizing glass produces isochromatic fringes in some transparent materials. When load is increased on a material, the fringe patterns change based on the amount of stress received. Because the sample and the bladder were both transparent, the fringes could be seen in both materials. In one test, the fringes were observed in the sample and in the bladder simultaneously. In a second test, a piece of paper was placed between the bladder and the sample to reveal the fringes developed in the sample only. A CCD camera, one of the DIC cameras, was used to record the changes in fringe patterns.

To quantitatively map the uniform pressure application, validations tests were performed on aluminum tubes. In the first test it was desired to know whether the pressure was applied uniformly around the sample. A 28 mm long 6061 aluminum tube was equipped with two sets of strain gauges which were installed on the outside wall, Figure 2.5. Two of the gauges were measuring strains in hoop direction and the other two gauges were measuring axial strains. The gauges were installed in the middle section of the sample to avoid the lip effect which is described in section 2.6.

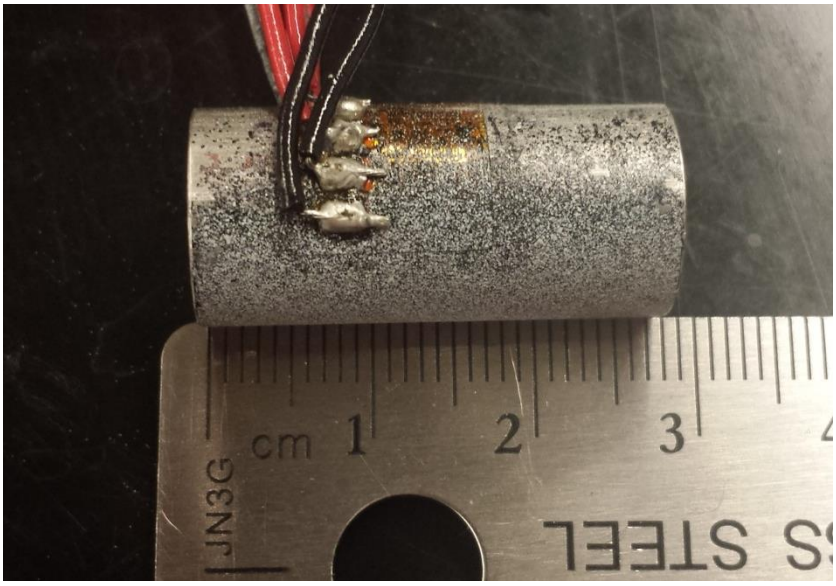

Figure 2.5 Aluminum validation sample with two sets of strain gauges bonded to the surface.

Using the bladder tube as an oil seal offers no limitations in regards to the length of a sample that can be tested (other than practical restrains). To verify that the length of a sample has no impact on uniformity of the pressure application, a 304 mm long 2024 aluminum tube was tested. It had three strain gauges installed in the hoop direction at locations 50.8 mm, 152.4 mm, and 254 mm along the axis of the tube as shown in Figure 2.6. One stain gauge was glued in an axial direction placed at 152.4 mm. Axial forces were minimized by positioning the alignment bars so the samples could be rotated freely by hand before the start of the tests. Both samples had 12.73 mm OD and 7.92 mm ID. The tubes were loaded in several loading-unloading cycles.

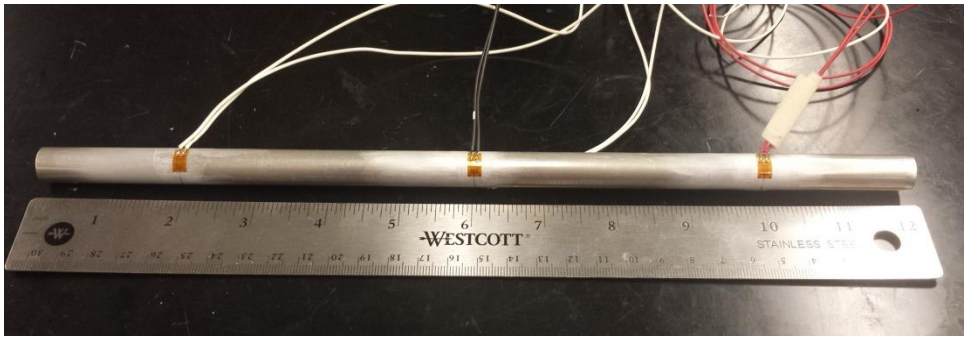

Figure 2.6 Aluminum validation sample with three strain gauges bonded in hoop direction and one strain gauge in an axial direction (away from the camera).

For all the tests done on the open-end and the closed-end burst rigs a thick-walled pressure vessel equation was used to calculate sample stresses on the outer (Equation 2.1) and inner surfaces (Equation 2.2):

$$\sigma_o = \frac{2 \cdot r_i^2 \cdot P}{(r_o^2 - r_i^2)} \qquad \text{Equation 2.1}$$

$$\sigma_i = P\frac{r_o^2 + r_i^2}{r_o^2 - r_i^2} \qquad \text{Equation 2.2}$$

where σ_o is the stress on the outer surface, σ_i is the stress on the inside surface, r_i and r_o are the internal and the external radii and P is the internal pressure. The outside wall stress was used to produce the stress-strain plots since the strains were all measured on the outer wall of the samples. The inside wall stress is import to consider since the maximum stress experienced by the samples is on the inside wall.

2.5 Closed-end Burst Rig Validation

For the closed-end burst rig it must be validated that a whole specimen undergoes a near uniform hydrostatic loading when pressurized. For this test a blind hole was drilled into a polycarbonate solid rod. The remaining portion of the rod acted as a

plugged end. The plug shape matched the end of the drill which has a standard point angle of 135°. A metal cone was bonded to the open end of the tube to provide the necessary axial support. Because of the mixed stress state in the material near the plug, the DIC system was used to measure the strain map along the axial direction of the sample.

To validate the experimental results, a 2D Finite Element (FE) model was generated in Abaqus 6.13. For this study a 2D axisymmetric model was created with isotropic and homogeneous material properties. Small strain approximation was used for these models as the stains in this material were measured below 1%. The Young's modulus and the Poisson's ratio were assumed to be 2.20 GPA and 0.31, based on literature data. The dimensions of the sample used for the model are shown in Figure 2.7 where the dashed line represents the axis of symmetry. The boundary conditions are shown in Figure 2.8. Horizontal line in the plugged section, which is 1 inch long, was restricted to move in Y direction only. On the other end of the sample a vertical line was restricted to move in X direction only representing the supporting force of the sample support cone. A pressure load of 6.9 MPa was applied on all of the internal surfaces of the sample. The finite element mesh was adjusted to minimize element distortion and is shown in Figure 2.9. An eight node, biquadratic axisymmetric quadrilateral element (CAX8R) was used with a reduced integration. The approximate element size was 0.51 mm.

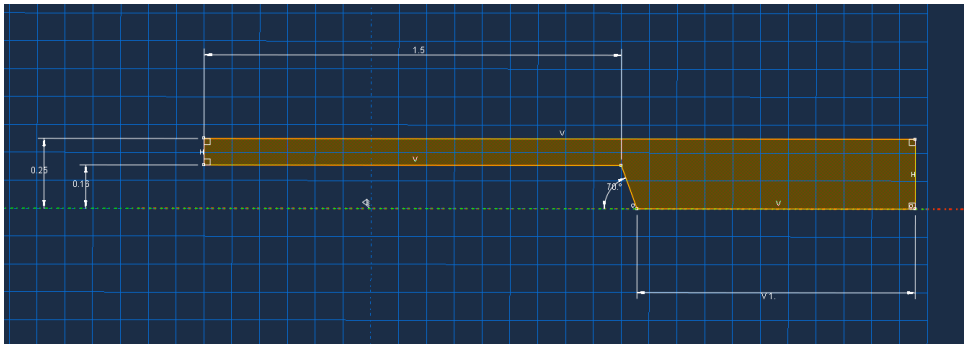

Figure 2.7 Dimensions of the end plug FE model.

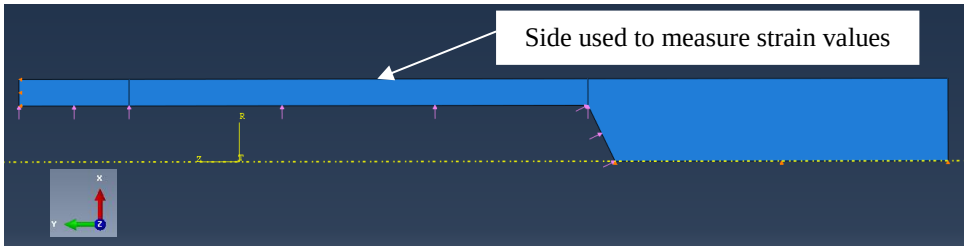

Figure 2.8 Boundary conditions for the end plug FE model.

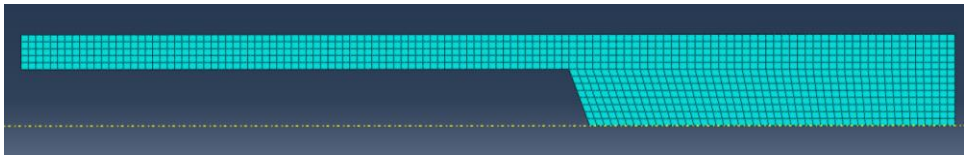

Figure 2.9 Mesh of the closed-end FE model.

2.6 Lip Effect Study

In the burst rigs described previously, a tested sample is supported and aligned in the rig with an adapter lip, Figure 2.2 (c), which is a thin wall extrusion located between the sample and the bladder. The lip also serves as a stress relief for the sample edges, avoiding edge induced failure. The effect of the length of the adapter lip had been studied by performing pressure loading tests with lip lengths of 2.5 mm, 5.1 mm and 7.6 mm. It is important to note that the lip must not deform more that the sample, crack or

breakoff. The DIC system was used to measure the strain variations along the axis of the samples. Polycarbonate plastic was chosen as the specimen material due to its high ductility and low elastic modulus producing high strain values. Large deformations can be measured more accurately with the DIC system. The samples had 12.9 mm outside diameter, 9.7 mm inside diameter and a length of 63.5 mm. After correlating the stress generated by the internal pressure to the strains measured by the DIC, a typical stress-strain curve was plotted to estimate the Young's modulus for the FE model.

A 3D finite element model was produced in Abaqus to simulate strains generated by the pressure. A quarter of a sample was modeled to reduce the computational time. The specimen dimensions in the model matched exactly the dimensions of the samples. The left, right and top sides of the sample were constrained to move in their perspective plains only, as shown in Figure 2.10. The internal surface of the sample was set to be pressurized to 6.8 MPa except the area that is protected by the lip. The sample mesh was generated using a 20 node quadratic brick type hexahedra elements (C3D20R) with a reduced integration. The approximate size of an element was 0.2 mm as shown in Figure 2.11. The resulting strain values were plotted along the middle of the model as shown in Figure 2.11. The experimental strain values were then compared to the FE results.

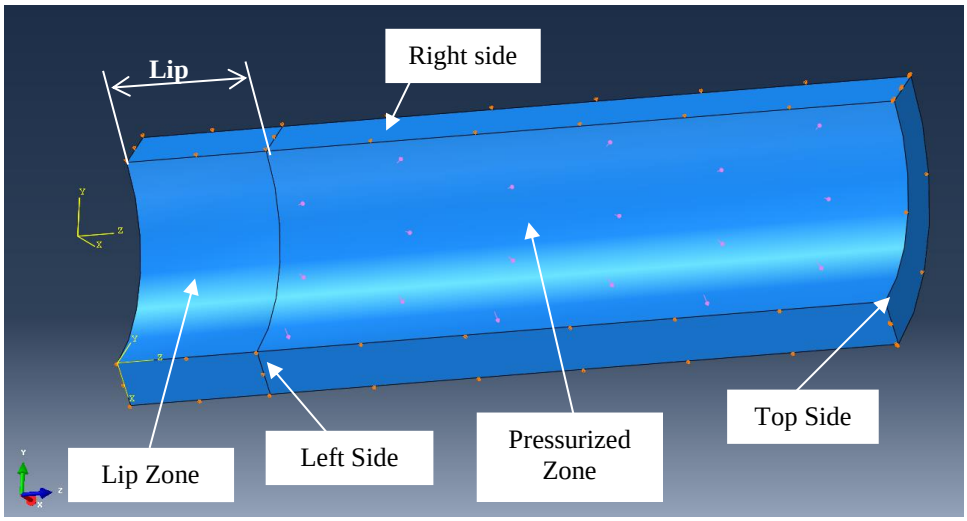

Figure 2.10 A 3D model of for the lip study with the boundary conditions.

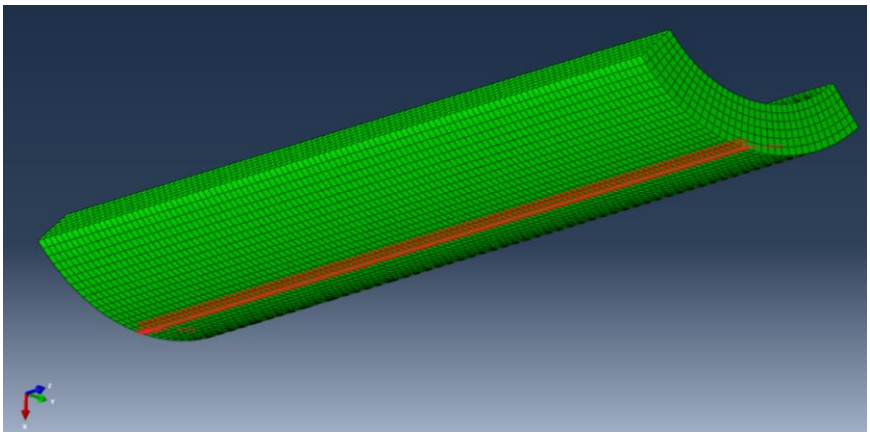

Figure 2.11 FE model showing path, in red, along which hoop strain values are plotted and the quadratic order elements.

2.7 Testing of SiC_f-SiC_m Composites

The SiC_f-SiC_m composite tubes were fabricated by General Atomics (GA). The samples were produced from Tyranno SA3 silicon carbide fibers coated with pyrolytic carbon interface layer. The matrix was formed by chemical vapor infiltration (CVI). A detailed description of the composite fabrication can be found in [34]. On average, the samples had 10.30 mm OD and 7.80 mm ID. Two types of fiber architecture were tested:

architecture A was slightly hoop reinforced with axial tow reinforcement and architecture B was strongly hoop reinforced. The samples of A architecture were tested in both the open-end (32 mm long) and the closed-end (63 mm long) burst tests. Architecture B samples were tested in the closed-end burst test (63mm long) only. All samples had been speckled for the DIC measurement and one sample for each of the test-architecture configurations had been equipped with 2 sets of strain gauges in the middle of the pressurized zone. In some tests, the samples were loaded straight to failure while most of the tests were loaded in several loading-unloading cycles gradually increasing the peak pressure. The end plugs for the closed-end burst tests were produced by depositing a 30 MPa shear stress J-B Weld epoxy. The cylindrical shape of the plug had a flat surface on the inside of the samples, similar to the plug shown in Figure 2.4 (b). Stress-strain curves were plotted for each of the samples. The stress was calculated using a thick wall pressure vessel equation. When using DIC, strain values were measured in the middle portion of the pressurized zone which was away from adapter lips and the support cone for the end plug samples. A typical surface area monitored by DIC was approximate 30% of the outside surface area.

2.8 Acoustic Emission Analysis

When analyzing AE, it has been noticed that with increased amount of damage in SiC_f-SiC_m, some AE parameters tend to change throughout a test, especially amplitude. To study the amount of change of these parameters, a 152 mm long SiC_f-SiC_m sample was tested in an open-end burst rig to a pressure above PLS with several loading-unloading cycles. As a part of another concurring test, after each cycle the sample was partially dismounted from the rig and the bladder tube was stretched out to avoid any

contact with the sample. Two Nano30 sensors were placed on either end of the sample after each cycle with an average distance between the sensors of 85.6 mm. Four or more pencil lead break tests were performed on the sample before the first loading and between each of the loading cycles. An average of each of the AE parameters collected from the lead breaks was calculated after every cycle.

CHAPTER 3. RESULT AND DISCUSSION

3.1 Open-end Burst Rig Validation

Images captured during the photoelasticity tests are shown in Figure 3.1. The photoelasticity is based on a birefringence phenomenon observed in some transparent materials. When light rays pass through a material it exhibits two refractive indices. It is these two refractive indices that have a direct relationship to the two principal stresses and to the fringes observed in the material. At a constant thickness, the isochromatic fringes represent contours of maximum shear stress. The higher the fringe density, the higher maximum shear stress level a test material experiences. The fringe pattern and fringe order observed in these tests showed two stress peaks and a stress relief profile near adapter lips. Mosley [12] analytically derived the stress profile of the pressurized area along the axis of a sample, as shown in Figure 3.2. Images from the photoelasticity tests show that the hydraulic oil produces a very similar stress profile as the one derived by Mosley. There was a small stress overshoot near the ends of the pressurized area before leveling off at a constant value. Images (a), (b), and (c) show the stress in the bladder and in the sample when image (d) shows the stress just in the sample when the bladder was cover up.

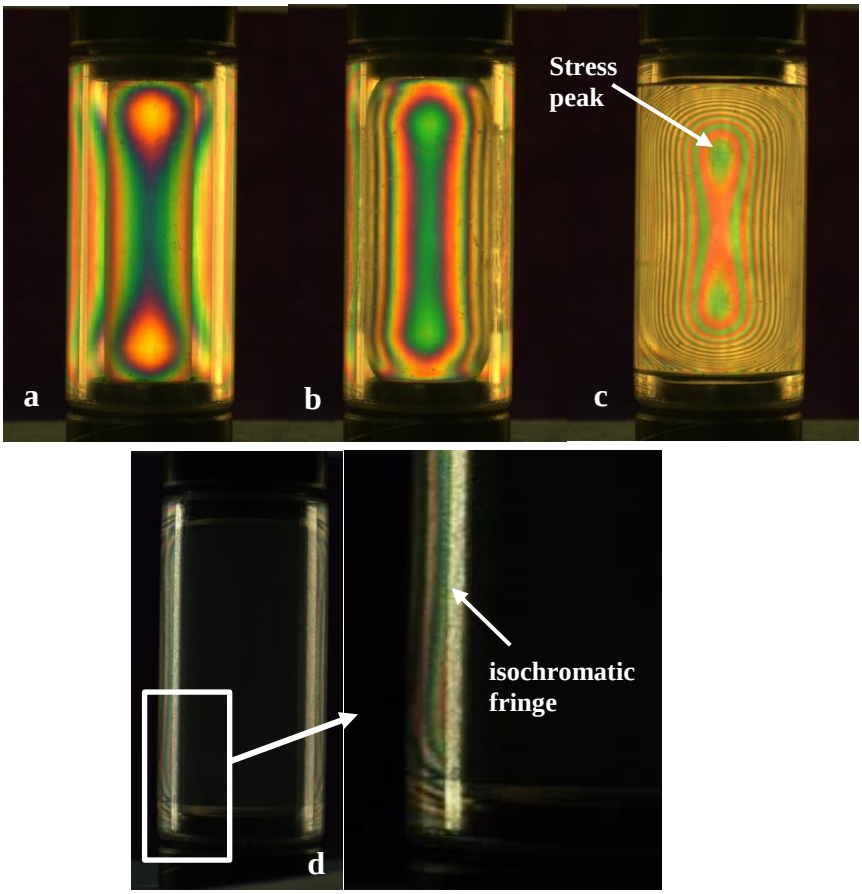

Figure 3.1 Photoelasticity test showing a specimen at (a) 0 MPa, (b) 0.9 MPa psi, (c) at 4.1 MPa and (d) at 4.1 MPa with the bladder covered.

The bladder behavior in the initial stages of a pressure loading was observed through the sample. Figure 3.1 (b) shows the bladder tube starting to deform during an initial contact with the internal surfaces of the specimen. This is indicated by a darkened surface on the sample. At this point there was still a large radius between the adapter lip and the sample. However, further increase in pressure deformed the bladder more severely forcing it to fill up the entire empty volume as shown in Figure 3.1 (c).

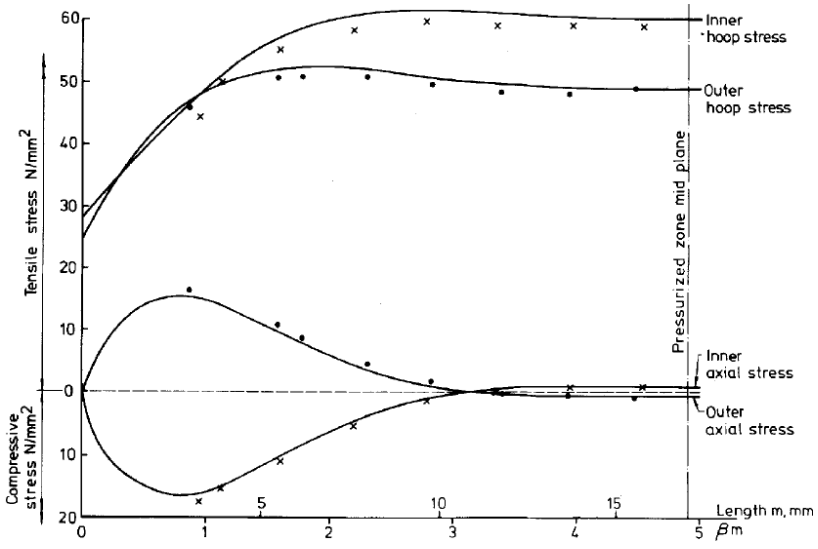

Figure 3.2 Mosley's analytical solution of the stress distribution where βm represents a non-dimensional length with the $\beta m=0$ representing the beginning of the pressurized zone [12].

To further evaluate the pressure uniformity, aluminum samples instrumented with strain gauges were tested. For the short, 28 mm long, sample the strains measured around the circumference and the calculated strains came very close together. Hoop strain values for one of the loading cycles are shown in Figure 3.3. An averaged difference between the two hoop gauges was 18.6 με and the two axial gauges was 8.0 με. Calculated Young's modulus and the averaged Poisson's ratio for this material measured at 71.55 GPa and 0.33 respectively, or 3.85% and 0% away from the published values. The percent error between the measured pressure and the pressure calculated from the sample strains is shown in Figure 3.4 and it is superpositioned against the oil pressure. At low pressures, the error values were large due to low strain values of aluminum. However, when the pressure was increased, the error values decreased. The graph shows that the error value is dependent on the internal pressure. For the first loading, at 22 MPa, the

majority of the error is within ±5%. When the pressure was increased to 62 MPa, the error value decreased to be between -1% and +4%. Similar calculation for the strains showed the percent error between the calculated and measured strain was within ±3% for the higher pressures. The errors were primarily attributed to the combined noise level from the strain gauges, and the acquisition system. Despite this noise, the results showed a uniform pressure loading around the sample and with a good agreement with the analytical solution.

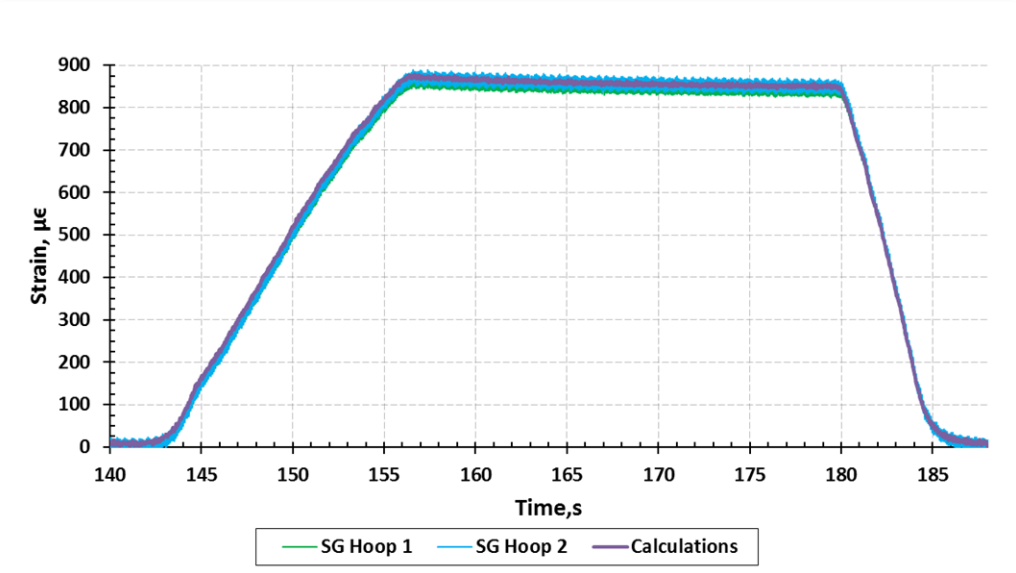

Figure 3.3 Strain values from 2 strain gauge readings and the calculated values for 28 mm long sample are plotted here.

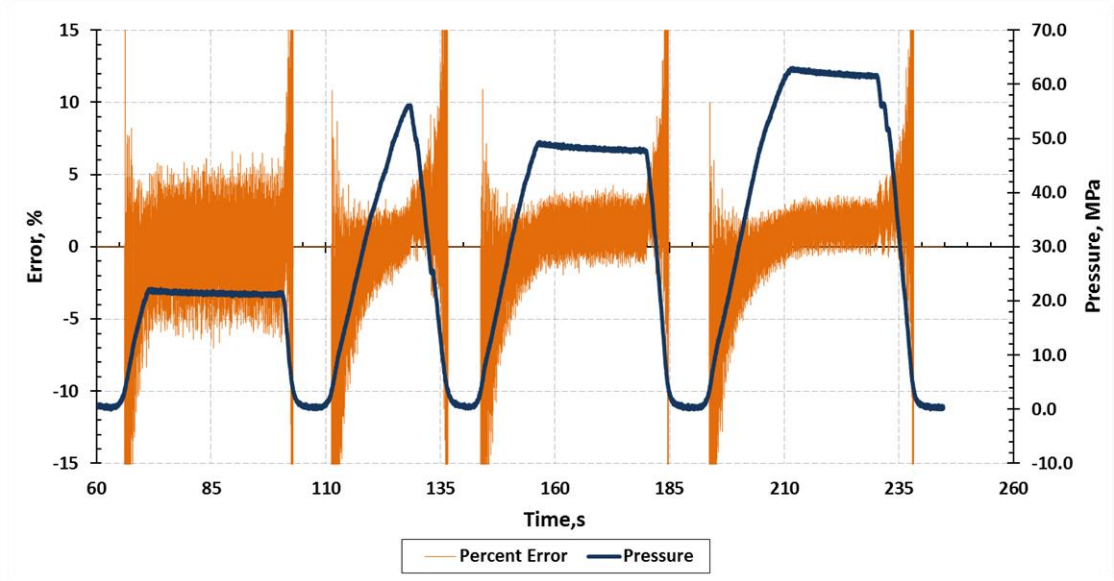

Figure 3.4 Percent error between measured pressure and the calculated pressure received by the 28 mm long sample.

For the longer, 304 mm long, aluminum tube, the same analysis was performed. The Young's modulus and the Poisson's ratio calculated to be 73.49 GPa and 0.32, which are 0.55% and 3% away from the published values. The percent error values for the last two high pressure loadings are shown in Figure 3.5. Similar to the 28 mm long sample, for the majority of the high pressure loading, the errors were within ±3%. Most importantly, the strain differences between the 3 hoop strain gauges were only 3 με at 62 MPa. The percent error between the calculated and measured strain values was within ±3%. These results proved that the bladder method can hydrostatically load a sample regardless of the sample's length.

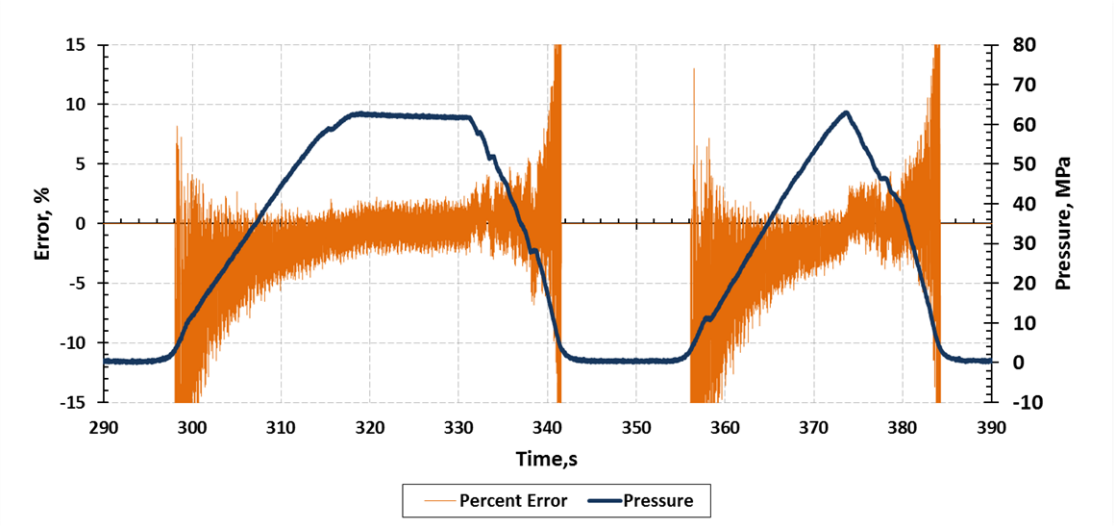

Figure 3.5 Percent error between measured pressure and the calculated pressure received by the 304 mm long sample.

3.2 Bladder Compressibility Effect

Pressurized oil naturally produces a uniform pressure on all the contacted surfaces. However, the addition of a bladder may affect the uniformity. It is important to consider the compressibility impact of the polymer bladder that may alter the amount of stress transferred to a sample.

Consider a solid block of material that is rigidly constrained from all sides except the top surface which has a pressure force with a resultant force P, Figure 3.6 (a). This approximation is meant to mimic and simplify actual loading condition experienced by the bladder as shown in Figure 3.6 (b).

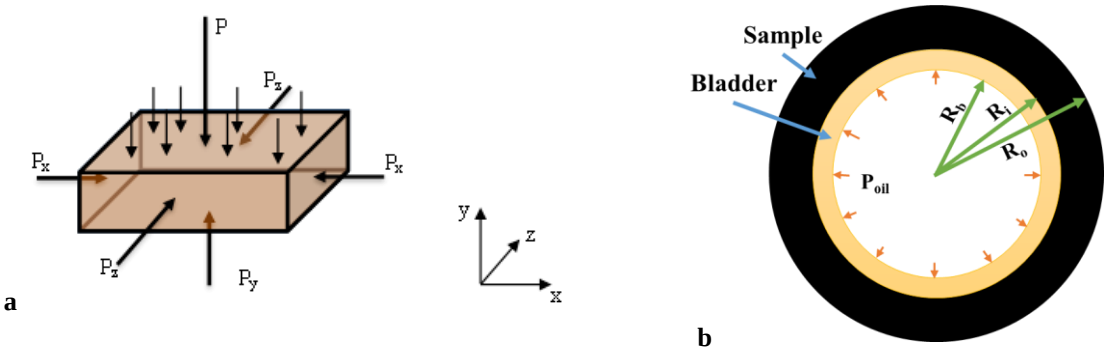

Figure 3.6 (a) Material constrained by all sides except top surface with a pressure force acting on the top surface; (b) Schematic of the bladder inside of a sample.

If the forces on the solid block act in x directions only, then, for an isotropic material, the strain in that direction according to solid mechanics equals to:

$$\varepsilon_x = \frac{1}{E}\left[\sigma_x - v(\sigma_y + \sigma_z)\right]. \qquad \text{Equation 3.1}$$

Strain in x direction equals to zero because of the rigid constrains in that direction. Stresses in x and z directions are the same, and since the stress on a surface equals to the pressure force, the equation can be rewritten in the following form as a function of applied force P:

$$P_x = \frac{v}{1-v}P. \qquad \text{Equation 3.2}$$

When considering forces in x direction only acting on one half of the bladder tube, as shown in Figure 3.7, all the forces can be summed up including the force on the bladder thickness, P_t, and the force of the interface between the bladder and the sample, P_{inf}. The resulting equation equals:

$$P_{inf} \cdot 2 \cdot R_i = P_{oil} \cdot 2 \cdot R_b + P_t \cdot 2 \cdot t. \qquad \text{Equation 3.3}$$

After simplifying the equations and substituting Equation 3.2 as P_t, the following final equation is obtained:

$$P_{inf} = P_{oil} \cdot \left[\frac{1-2v}{1-v} \cdot \frac{R_b}{R_i} + \frac{v}{1-v}\right]. \qquad \text{Equation 3.4}$$

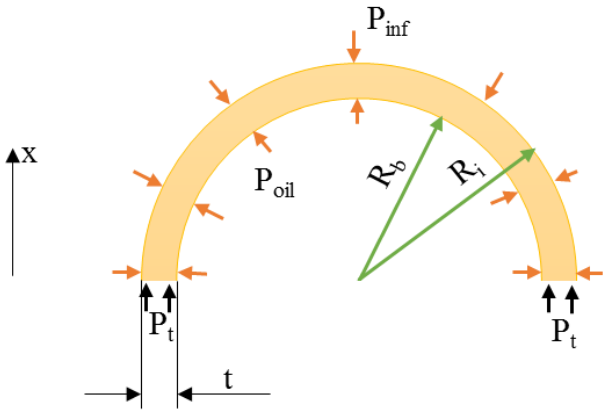

Figure 3.7 Representative forces on the bladder in x directions.

The above equation shows that the amount of stress/pressure transferred through the polymer bladder depends on the thickness of the bladder, t, and the Poisson's ratio of the polymer. Therefore, when the Poisson's ratio is 0.5, all the pressure is transmitted to the sample regardless of the bladder thickness. When the Poisson's ratio is less than 0.5, the thickness of the bladder produces additional reduction in the transmitted pressure. When the bladder thickness is negligible, $R_b \approx R_i$, the Poisson's ratio has negligible effect and the full pressure is transferred to the sample.

The Poisson's ratio of the actual bladder was not measured. However, when considering aluminum tube testing discussed in a section 3.1, the Poisson's ratio is the only unknown in the Equation 3.4. Therefore, it could be estimated from the inverse of the above formula:

$$v = \frac{\frac{P_{inf}}{P_{oil}} - \frac{R_b}{R_i}}{1 - 2 \cdot \frac{R_b}{R_i} + \frac{P_{inf}}{P_{oil}}}. \qquad \text{Equation 3.5}$$

For the 304 mm long sample, when restraining the values to be within 0 and 0.5, the resulting Poisson's ratio could be seen in Figure 3.8. The averaged value of the Poisson's ratio during pressure holding measured to be around 0.49 indicating that the bladder compressibility has a negligible impact. Similar Poisson's ratio was reported for a PVC (polyvinylchloride) polymer during cyclic loading [35].

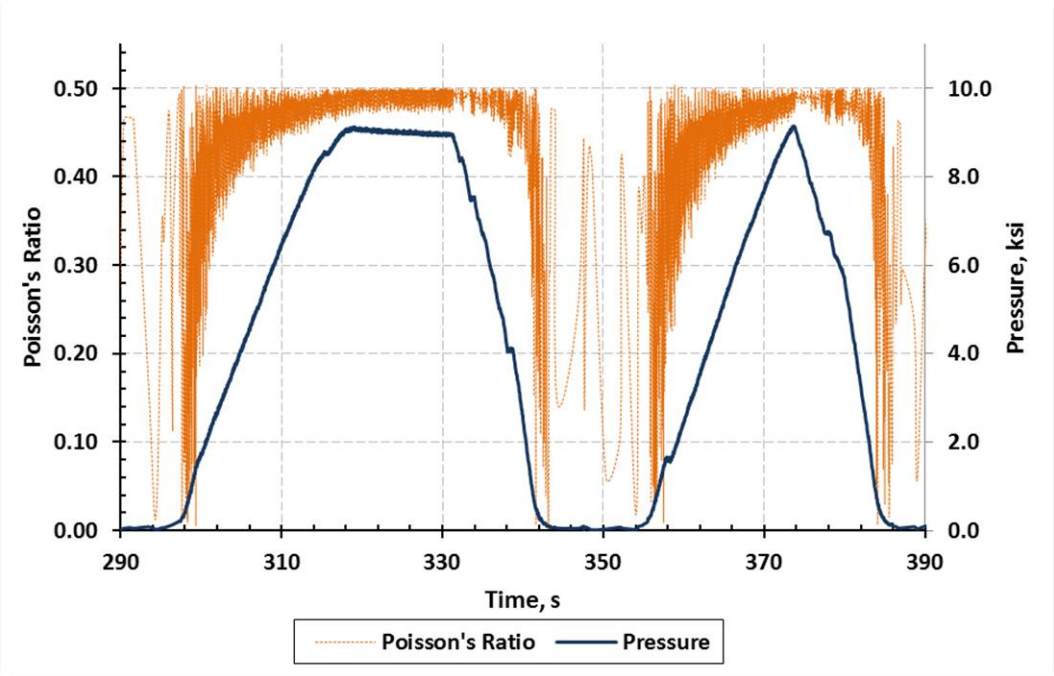

Figure 3.8 Poisson's ratio calculated from 304 mm long aluminum sample test.

3.3 Closed-end Burst Rig Validation

The test results of the closed-end burst test are plotted in Figure 3.9 along with the FE results. The strain values from FE analysis were extracted from the outer surface of the sample as indicated in Figure 2.8. The sample's plug extends from -12 to 0 mm. In

the hoop direction the strains have a gradual increase to a small amount of overshoot before leveling off, similar to Mosley's results. The axial strains, as expected, are also in tension which means a push out force was applied by the bladder plug against the sample. The strain values between the experimental and simulation results came relatively close to each other, however, a small variation is present. It would be expected that the literature values for the Young's modulus and the Poisson's ratio used for the modeling might be different from the ones of the actual material causing the shift. On the other hand, these results provided the necessary assurance that the polymer end plug method produces hoop and axial forces onto the sample in a desired near hydrostatic manner.

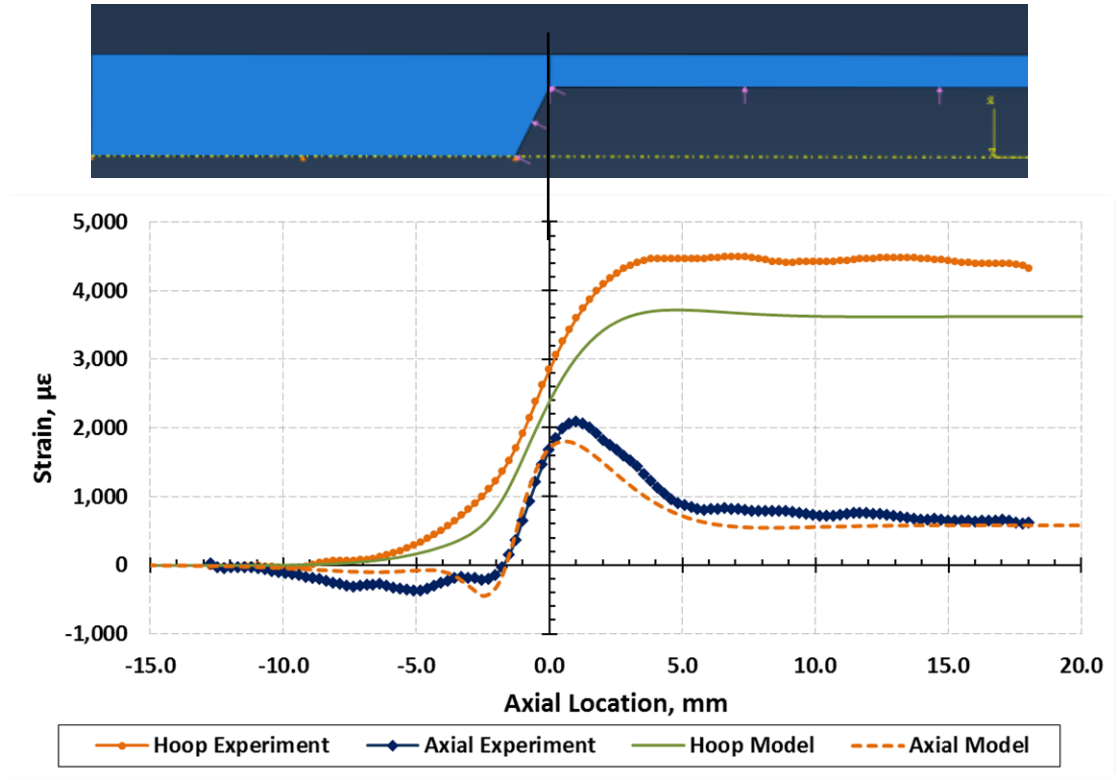

Figure 3.9 Comparison between measured and modeled strains in a closed-end sample. Zero inches indicates the edge of the plug in the sample.

3.4 Lip Study

A small lip extending into the sample tube is a key feature to prevent the extrusion of the polymer bladder tube through the sample/fixture joint under high pressures. It also provides a way to reduce stress on the sample's edge. The lip study tests were performed to quantify the amount of the relieved stress and a lip effected zone. To avoid yielding of the polycarbonate specimens, the pressure chosen for these tests was 6.9 MPa. The DIC acquisition system was set to output the strain values along the sample's axis. The same was done in the FE model. The FE results for a 5.1 mm lip are shown in Figure 3.10, but similar results could be observed in the other two models.

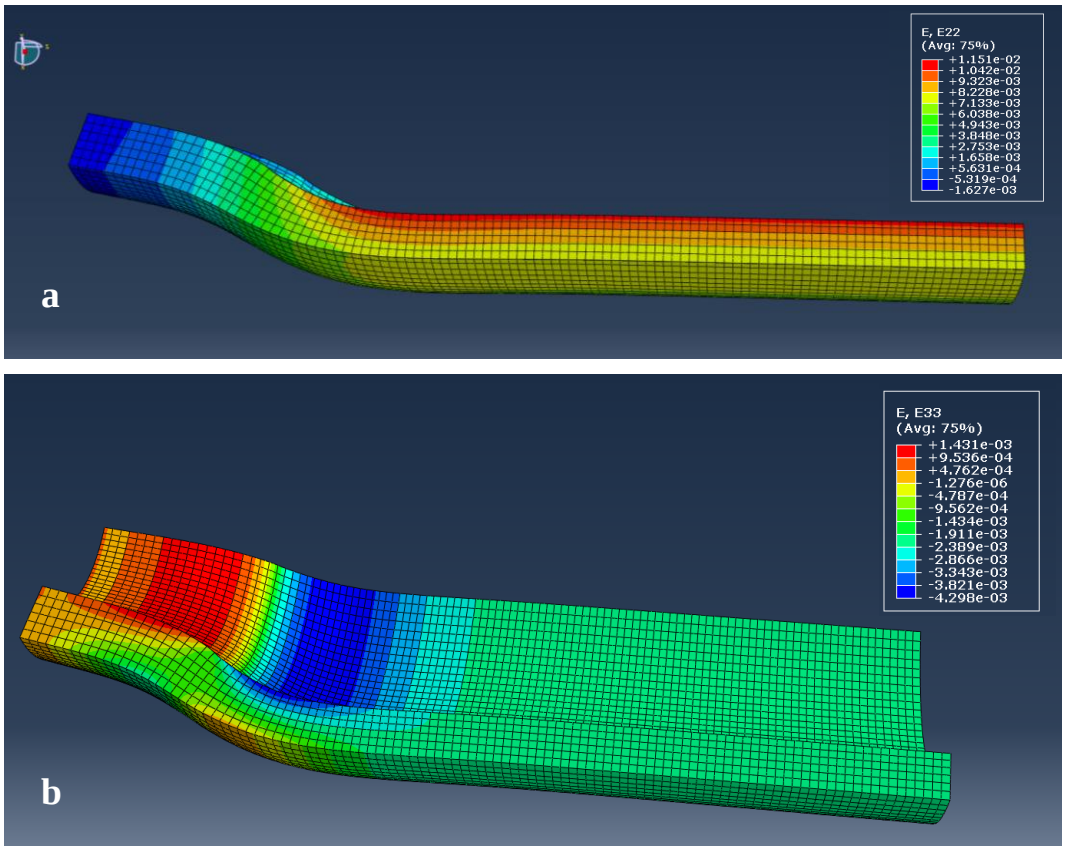

Figure 3.10 Typical results of a lip study showing exagerated deformation for (a) hoop direction strains and for (b) axial direction strains. An adapter lip is not shown but it would be present on the left side of the sample.

From the strains in the hoop direction, Figure 3.10 (a), the region with the highest stress is the inside wall of the sample, away from the lip edge. This behavior is in a good agreement with Mosley's analytical results when setting the edge of the lip to be the beginning of the pressurized zone. From the axial direction strains, Figure 3.10 (b), bending near the lip in the pressurized zone is observed through the exaggerated model deformation along with the compressive and the tensile strains. A bright blue band indicates compressive strains of up to -4300 με while through thickness tension strains are observed of 1000 με. Along with the high positive strain values in the hoop direction, it could be expected that this non-uniform stress state might be the failure initiation area for some materials.

Experimental and simulation results in both axial and hoop directions for the polycarbonate samples are plotted together in Figures 3.11-3.13. The experimental results matched well with the simulations, although a small offset exists. Photoelasticity test showed that the bladder at such low pressures may still have a small curvature between the adapter lip top surface and the internal surface of the sample. The small curvature is on the order of 0.51 mm and it was postulated that it was the reason for the shift between the experimental and the modeling results.

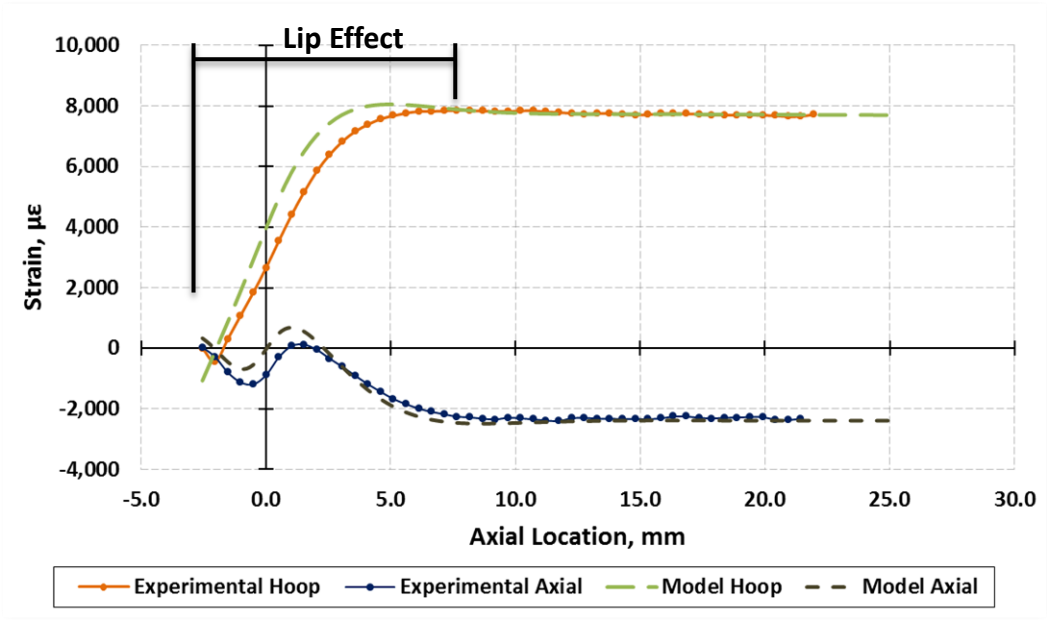

Figure 3.11 Comparison between calculated and measured strains for a 2.5 mm lip.

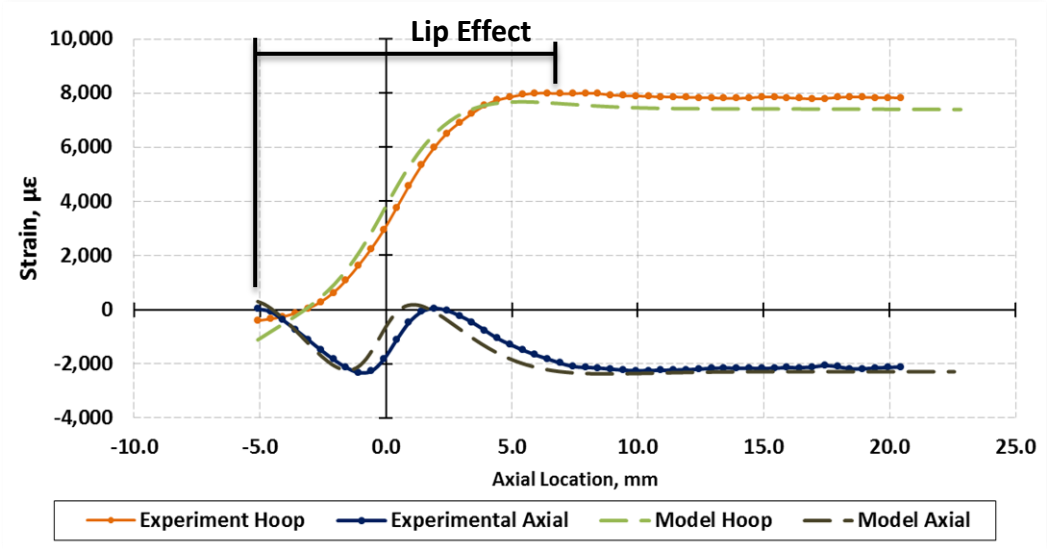

Figure 3.12 Comparison between calculated and measured strains for a 5.1 mm lip.

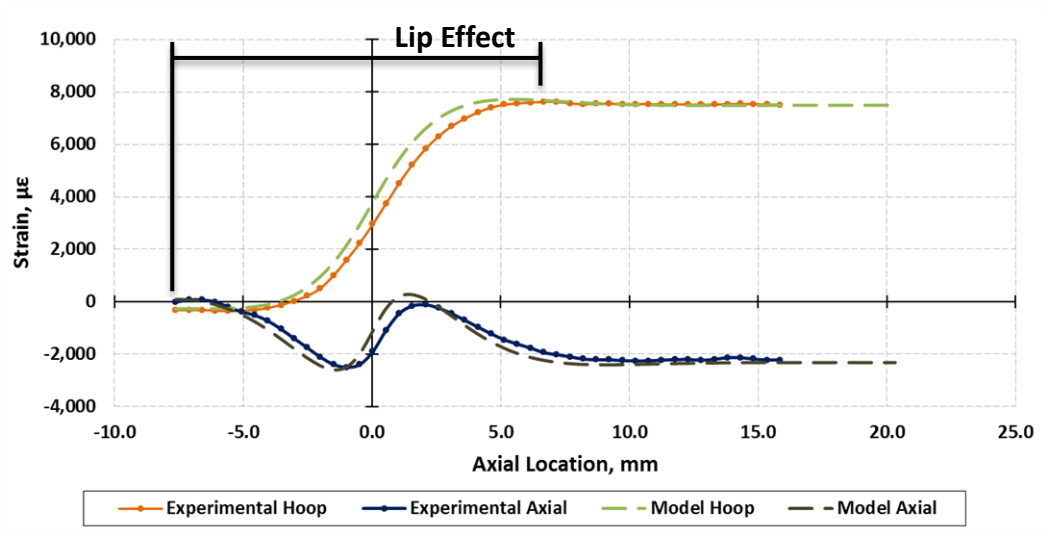

Figure 3.13 Comparison between calculated and measured strains for a 7.6 mm lip.

In the plots above, the edge of the sample shows a negligible amount of stress for all three lip lengths. Graphs show that the longer the lip the more gradual the increase in hoop strain is. For 5.1 mm and 7.6 mm long lips hoop and axial strains at 0 mm location are nearly identical. On the other hand, for the 2.5 mm lip the axial strains are noticeably lower. Also, the experimental result for the 2.5 mm lip, unlike for the other two, does not show a noticeable strain overshoot.

From the above analysis, it could be concluded that the 2.5 mm long lip is an adequate length for isotropic materials. It allows using a shorter test sample, does not have as much of the axial strains at the lip edge versus the longer lips and it shows lower to no overshoot just pass the lip. For all tests reported in this work, a 2.5mm long lip was used.

3.5 Mechanical Testing of SiC_f-SiC_m Composites

A total of 12 samples of A architecture were tested in the open end burst rig, three samples of A architecture were tested in the closed-end burst test and three samples of B architecture were tested in the closed-end burst rig. Young's modulus, E, internal surface stresses, σ_i, outside surface strains, ε_o, internal pressures, P, and an apparent end plug pushout forces, F, are summarized in Table 3.1. During the analysis, a PLS point was first identified from the stress-strain curve. The data presented here was performed on B-A-4 specimen and is representative of the sample set.

It is important to note that the strain maps of these composites are highly non-uniform. DIC provides a full-field strain map and showed evidence that the difference in strains from point to point can be 4,000 με or larger right before the failure, as seen in Figure 3.14. The regions R1 and R2 were purposefully chosen in high and low strain regions respectively. This behavior is not obvious when using a single strain gauge.

Also, because of the large variations in strains from point to point, it is evident that even the stress-strain curves and all the parameters calculated from it (PLS, Young's modulus, etc.) can differ significantly. For example, Figure 3.15 shows three stress-strain curves produced by using three different size and location strain regions. For this study the largest reasonable width was used including both, the high strain regions and the low strain regions, just like R0 in Figure 3.14. The regions were also chosen in the central portion of the axial direction to avoid edge effects of the adapter lips. This edge effect can be seen in Figure 3.14 as the high strain regions in red are diminished to the left of the image where the adapter lip is. The long and narrow high strain bands also appear to have some correlation to the fiber architecture.

Table 3.1 SiC_f-SiC_m test results: values shown in parenthesis are obtained from strain gauges; all other values are obtained from DIC data.

Sample	Test (Architecture)	at Proportional Limit Stress				At Ultimate Stress			
		E_0^{pls}, GPa	P^{pls}, MPa	σ_i^{pls}, MPa	ε_0^{pls}, με	P^{max}, MPa	σ_i^{max}, MPa	ε_o^{max}, με	F^{max}, N
B-A-1	Burst (A)	184	32.0	118	500	105	377	n/a	n/a
B-A-2	Burst (A)	167	35.1	133	590	93	347	6,023	n/a
B-A-3	Burst (A)	170	32.8	125	510	105	404	8,271	n/a
B-A-4	Burst (A)	224 (184)	31.5 (25.0)	127	420 (420)	98	391	7,525 (8,636)	n/a
B-A-5	Burst (A)	158	31.2	116	530	111	372	n/a	n/a
B-A-6	Burst (A)	171	32.0	121	480	90	340	6,299	n/a
B-A-7	Burst (A)	217	37.0	142	520	102	392	7,115	n/a
B-A-8	Burst (A)	n/a	n/a	n/a	n/a	100	369	n/a	n/a
B-A-9	Burst (A)	174	28.8	111	505	95	367	8,238	n/a
B-A-10	Burst (A)	n/a	n/a	n/a	n/a	95	374	n/a	n/a
B-A-11	Burst (A)	182	31.1	119	500	99	379	8,978	n/a
B-A-12	Burst (A)	198	31.4	122	510	108	418	8,565	n/a
E-A-1	End plug (A)	179	38.6	142	580	95	352	6,523	4,554
E-A-2	End plug (A)	167	31.4	115	560	100	368	9,111	4,792
E-A-3	End plug (A)	195 (202)	35.3 (38.3)	134 (143)	500 (560)	101	380	7,089 (6,273)	4,881
E-B-1	End plug (B)	190	34.7	134	530	52	203	1,172	2,607
E-B-2	End plug (B)	184	33.3	129	515	47	175	925	2,296
E-B-3	End plug (B)	159 (206)	34.3 (38.0)	125 (134)	560 (475)	58	212	1,834 (1,138)	2,860

However, a care should be taken when interpreting strain maps, especially near uncorrelated regions as strain values in these regions are less reliable due to the smoothing algorithms. The regions with unreliable measurements can be detected when excessively high or low strain values are shown. In those cases the strain were considered to be an outlier and were not included in the specimen analysis. The majority

of the uncorrelated regions were due to inherent roughness of the samples making it difficult to properly speckle and illuminate. Nevertheless, the DIC strain maps can give a good representation of the loading state of these samples.

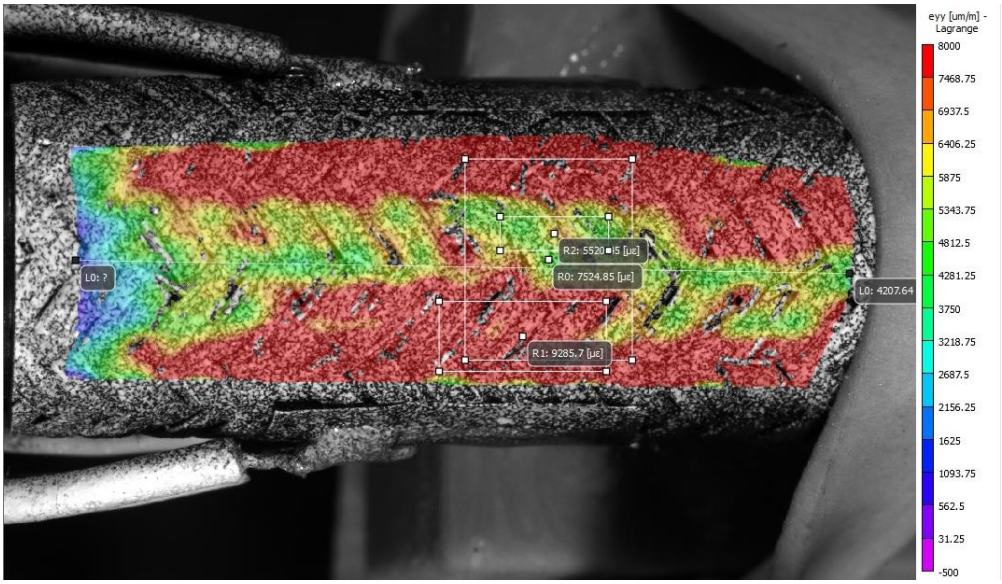

Figure 3.14 Typical DIC strain map showing three regions with their corresponding average hoop strain values and some uncorrelated areas.

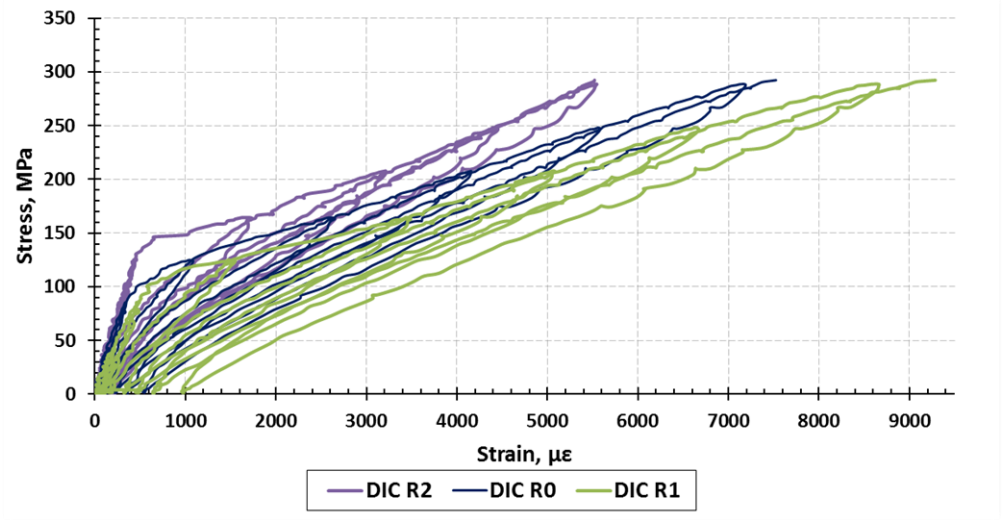

Figure 3.15 Three stress-strain curves are made from different regions of the same sample with R2 region having the lowest averaged strain which corresponds to the highest PLS.

Loading-unloading pressure cycles showed a strong hysteresis behavior in the inelastic portion of the curve. The hysteresis indicates presence of matrix cracking and interfacial fiber-matrix sliding [9]. Vagaggini et al. also mentioned that unloading and reloading paths should be symmetric. However, when the unloading path deviates from the symmetry it indicates that the crack surfaces created from the initial opening are closed during unloading making a surfaces-to-surface contact. This behavior is seen in these samples as shown in Figure 3.16. When deviating from symmetry, the unloading path crosses the hysteresis modulus line which is shown as a dash line. The final failure of the sample indicated fiber pullout visible by a naked eye supporting a weaker fiber-matrix bond condition. Certain amount of fiber pullout is desired for composite materials. The wavy behavior during second unloading in Figure 3.16 was due to the manual hydraulic pump operation as it becomes increasingly difficult to manually pump the oil. Vagaggini had also suggested that the reloading path should go through the same maximum stress-strain point that was reached before the unloading. While it appears to be true for the first loop, which is still undoubtedly in the stress state between the PLS and the crack saturation studied by Vagaggini, it is not so for the second loop. For the second loop the reloading path reaches the same stress state but with additional 200 με. This behavior is consistent with other SiC_f-SiC_m composites in literature [37].

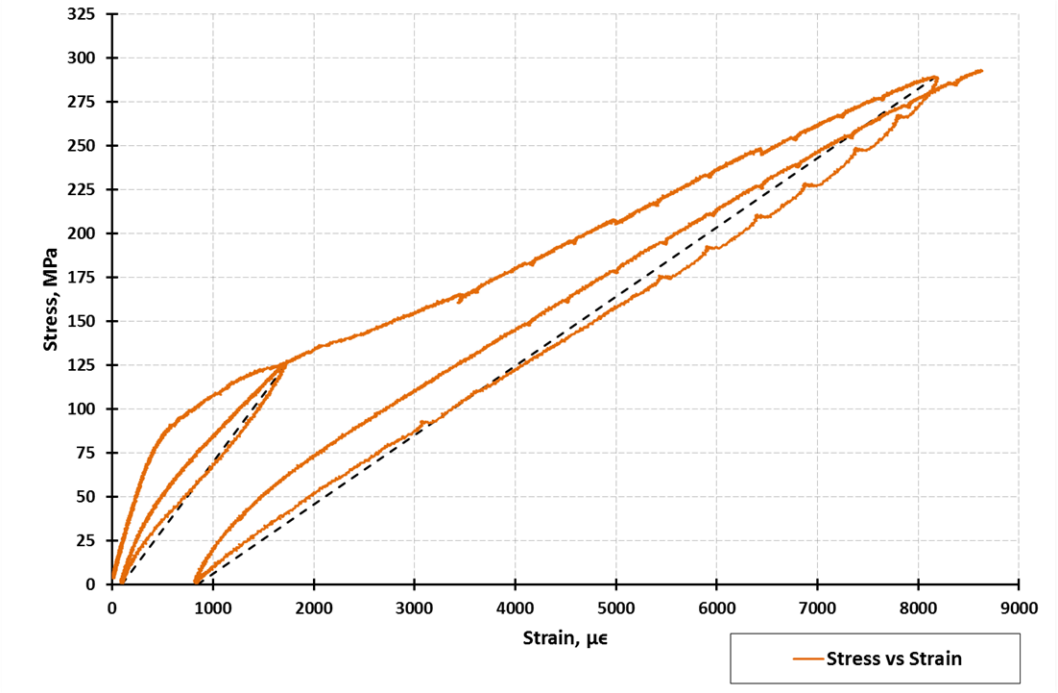

Figure 3.16 Stress-strain curve showing only two unloading cycles. The wavy part during second unloading is due to manual pump operation. The unloading path crosses hysteresis modulus (dashed line) indicating matrix crack closure.

From testing A architecture samples, the open-end burst and closed-end bust tests produced equivalent results. This suggests that the forces in hoop direction play the major role in material failure during internal pressurization. These samples also showed good performance with the failure at internal pressure averaging at 99.8 ±5.6 MPa, inside wall stress of 375.5±20.1 MPa, and Young's modulus of 178.8±15.8 GPa. Samples of B architecture produced similar stress and strain values at PLS, and Young's modulus, but the failure pressure was twice as low at 52.2±4.6 MPa. Samples B were expected to produce higher failure pressures because of the greater fiber reinforcement in the hoop direction. However, B samples did not show visible fiber pullout suggesting that the fiber-matrix interface was stronger, therefore, the specimens were more brittle than

sample A. However, contrary to brittle monolithic tubes, both types of samples ruptured with little fragmentation retaining most of its shape.

Jacobsen et al. from General Atomics tested similar samples produced by CVI methods with a Tyranno SA3 fiber and a pyrolytic carbon interface of less than 200 nm thick [7]. The test results showed samples with 282 GPa Young's modulus, 182 MPa PLS and 418 MPa ultimate tensile strength (UTS). These values are slightly higher than results obtained in this work, but some of the differences can come from the fiber architecture.

A Weibull analysis of A architecture samples was performed on a sample set of 12. PLS and UTS on the inside and the outside surfaces were evaluated with the resulting Weibull plots shown in Figure 3.17. The Weibull moduli for each of the data sets ranged from 15 to 21. The fairly high moduli indicates that the strength of the GA fabricated SiC_f-SiC_m composites have very low variability. It also suggests that the internal bladder test method produces repeatable loading stress state.

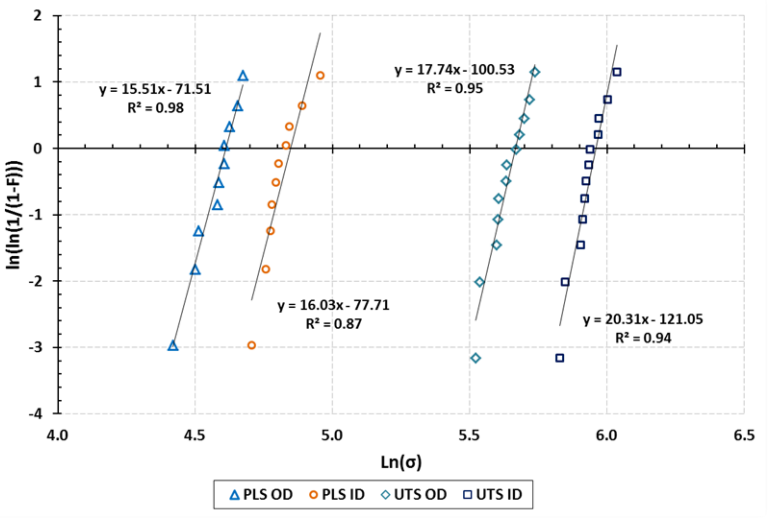

Figure 3.17 Weibull plots for the PLS and UTS.

In conclusion, consistent mechanical properties of SiC_f-SiC_m nuclear fuel cladding composites were obtained using the newly developed internal pressurization method. Architecture A samples exhibited good mechanical properties required for the use in LWR applications. In a simulated LOCA burst test [36], the pressure inside the cladding was found to rise to around 12 MPa and the Zircaloy-4 cladding temperature rose to around 800ºC in less than 50s. The Zircaoy cladding eventually burst under internal pressure due to temperature-induced material softening. In this study, the type A SiC_f-SiC_m composite tube can withstand over 8 times the maximum pressure recorded in the simulation and can potentially avoid breaching of the cladding under similar conditions. However, if fractured, the cracked composite cladding would still retain coolable geometry and thus keep the majority of the fuel pellets at their original location. With its higher temperature resistance, high strength and toughness, SiC_f-SiC_m composite cladding can potentially provide a greatly improved accident tolerance during LOCA condition.

It was also shown that the newly developed burst rig performed well with these composite samples. One of the advantages of the bladder method is that it prevented oil from leaking out even when testing porous or micro-cracked composites such as SiC_f-SiC_m. Also, while the internal surfaces of the samples were rough, the soft polymer tube filled in all of the cavities, which were observed in the bladder after the test. This suggests that as long as the internal surfaces are not sharp enough to cut the bladder, the polymer bladder can deform to a complicated texture still applying a hydrostatic pressure. This uniform contact would not be possible with a segmented mandrel method and potentially not with the polymer insert method, depending on the hardness of the insert.

3.6 Acoustic Emission Analysis

Acoustic emission data had been gathered as an additional source of information to help gain better understanding of the mechanisms happening in the material when it's stressed. The ultimate goal for using the AE is to be able to differentiate damage mechanisms based solely on AE signals. AE signal analysis revealed aspects about composites that have a potential to improve early damage accumulation detection, fabrication, and the clustering of Unsupervised Pattern Recognition analysis.

It had been noticed that the most AE activity and the highest AE amplitude signals are produced near or at PLS point (when excluding the highest signal during sample burst); Figures 3.18 and 3.19 show this well. This behavior was consistent enough such that determining the approximate time when PLS point had been reached could be done solely based on AE data. The AE activity rate also increases significantly at PLS. In addition, some time after PLS is reached, it was observed that the AE signal intensity decreases a substantial amount, as seen in Figure 3.19 after 74 seconds. Such behavior had been observed before. Morscher [26] had reported that AE energy attenuated the most when the SiC_f-SiC_m composite is under high tension stress state.

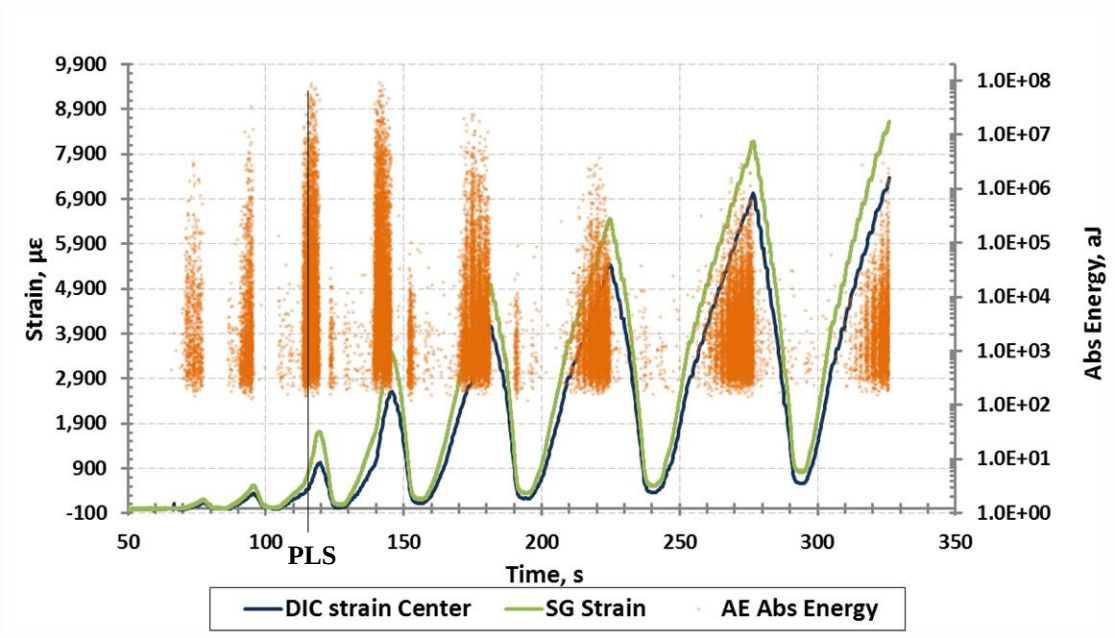

Figure 3.18 Acoustic Emission activity and intensity compared to sample strain for B-A-4 specimen.

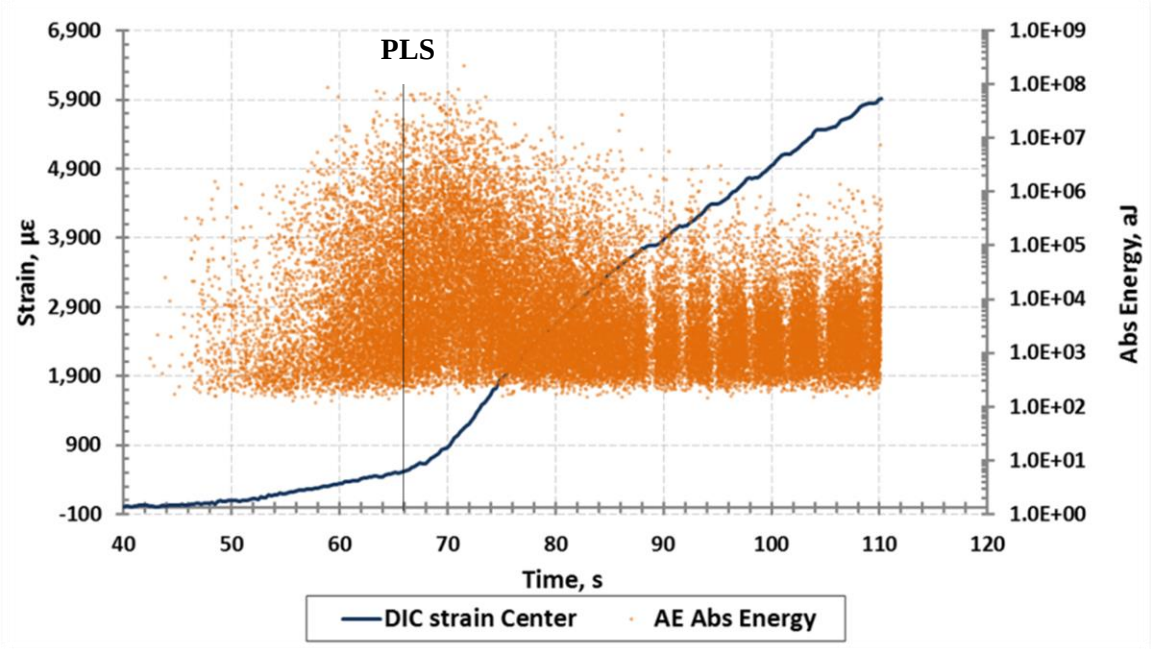

Figure 3.19 Acoustic Emission activity and intensity compared to sample strain for E-A-1 specimen.

Because of the above mentioned energy attenuation and high energy peaks at PLS, it is desired to know how other AE parameters change with increased amount of composite damage. The test setup for this study is described in section 2.8. The change in several standard AE parameters is shown in Figure 3.20. For clarity, only representative parameters of AE behavior are shown, as mentioned earlier, other parameters are related to these in the graph. All of the parameters are normalized with respect to values obtained from lead break tests before the sample was loaded. The PLS point was approximated based on AE intensity and activity as described earlier and was estimated to be between 15 and 17 MPa.

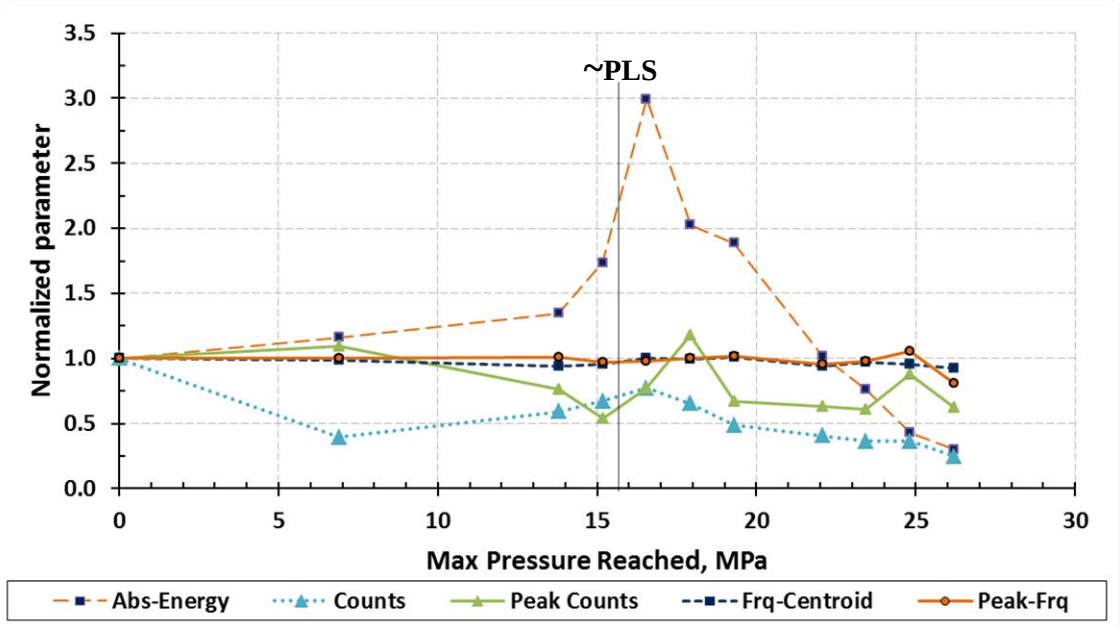

Figure 3.20 Normalized AE parameter change with respect to composite damage.

The above graph shows that most of the parameters change with increased amount of damage. Most parameters make large deviations from the initial values after reaching PLS. The number of counts reduced by over 50% changed after the first loading of 6.9

MPa. Nozawa [20] suggested that matrix cracking starts around 80% before the PLS but the 6.9 MPa reached during the first cycle is only around 50%. Absolute energy increased significantly after the PLS, but then dropped to below 0.3 of the initial value.

However, contrary to other parameters, peak frequency and frequency centroid parameters remained unchanged, Figure 3.20. Ono had stated that in carbon fiber reinforced polymer matrix composites frequency domain information is often times enough to identify composite damage mechanisms [31]. This case may apply to SiC_f-SiC_m composites as well, however, thorough investigation would be needed. To investigate this case further, a plot of peak frequencies for E-A-1 sample is shown in Figure 3.21. AE events appear to be grouped into bands at various frequencies. It should be noted, however, that the AE sensor used for this test has a resonant frequency at 300 kHz. Resonant frequency sensors are more sensitive to that particular frequency. Initially, six bands of AE signals could be seen in the graph. A frequency shift could be observed between 62 and 75 second with PLS being reached at 67 seconds. For example, band 4 on average had reduced from 229 kHz to approximately 195 kHz. The AE events in bands 1 and 5 initially lowered in frequencies but then seemed to merge with other bands of signals. Bands 2 and 3 appear to remain constant through the test, with band 6 also showing constant frequency but at the very edge of AE sensor sensitivity range.

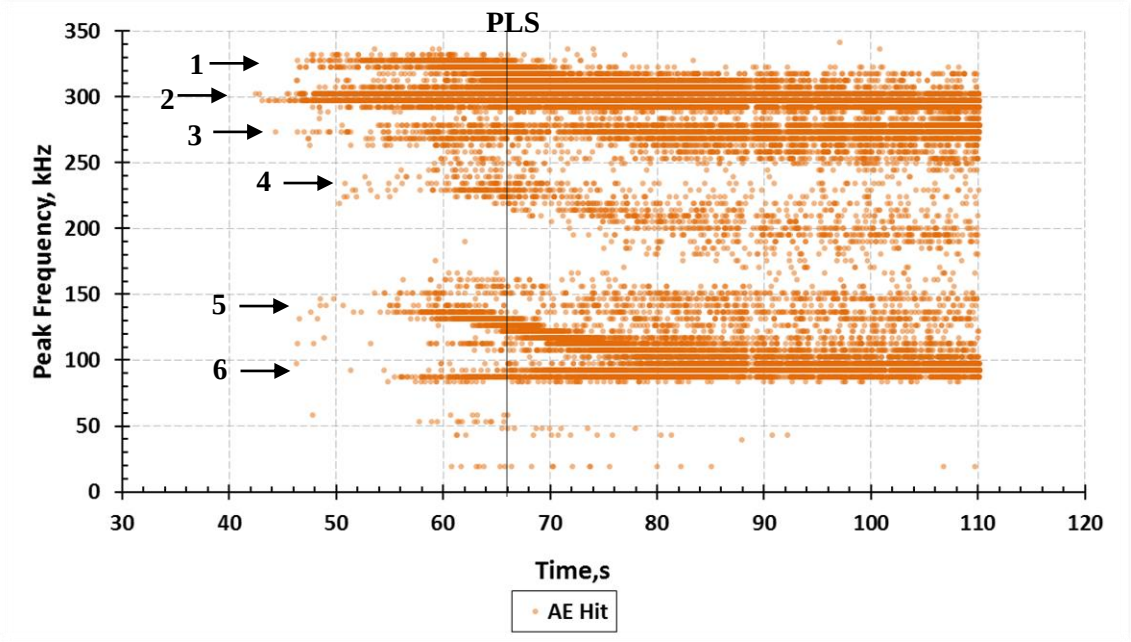

Figure 3.21 Peak frequencies for E-A-1 sample showing drifting of AE signals towards lower frequencies as damage progresses.

While additional testing is required to measure AE parameters change with increased damage; some initial conclusions could be made from the last two data sets. The lead breaks on undamaged and pass-PLS damaged sample had produced AE events with unchanged peak frequencies. Internal pressure burst test also produced two bands of AE events with seemingly unchanging frequencies. If AE signals in each, or some, of the peak frequency bands were produced by a specific damage mechanism, then just like for a carbon fiber polymer composites this information would be enough for a pattern recognition analysis. The second conclusion is that for UPR it would be best to use AE parameters that stay unchanged, such as frequency. As seen earlier, absolute energy and counts vary largely depending on the composite damage state. These factors can make clustering analysis more difficult if not addressed.

Another observation was made in regards to A type architecture SiC_f-SiC_m samples. Bursts of AE events were detected during unloading and after reaching PLS, as seen in Figure 3.18 around 125, 155 and 190 seconds. This behavior contradicts a commonly observed Kaiser and Felicity effects. The start of these bursts had been noticed to correlate with the time when the unloading path on the stress-strain curve had crossed the hysteresis modulus line in Figure 3.16. As discussed earlier, matrix crack closure and surface-to-surface contact are expected to take place during the unloading. This phenomenon is detected by a rapid increase in material compliance and observed exclusively in A type architecture samples. Therefore, AE bursts during unloading are believed to be signals detecting matrix crack surfaces closing up and making a contact. This information could be of a significant importance when doing pattern recognition analysis. A representative waveform of those AE busts is shown in Figure 3.22. For a comparison, the strain vs AE absolute energy for a sample with B architecture is shown in Figure 3.23.

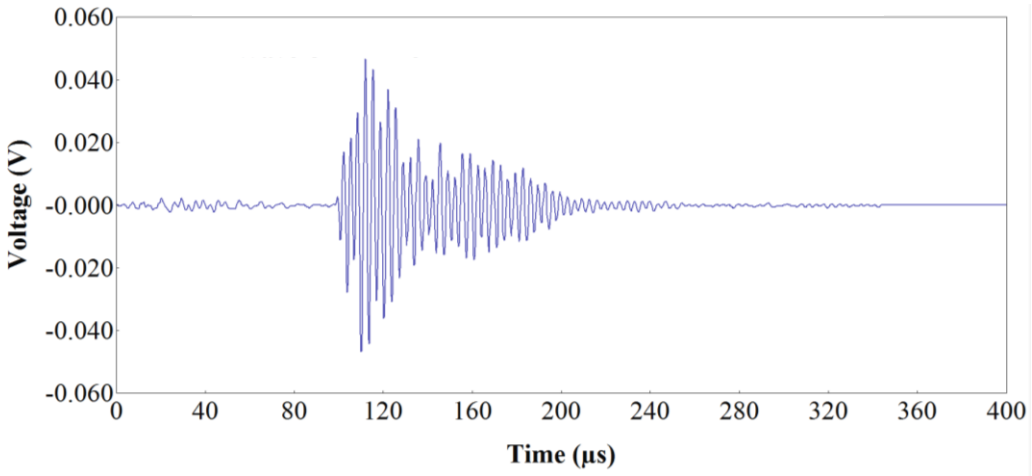

Figure 3.22 Typical AE signal associated with matrix crack surface-to-surface contact upon unloading.

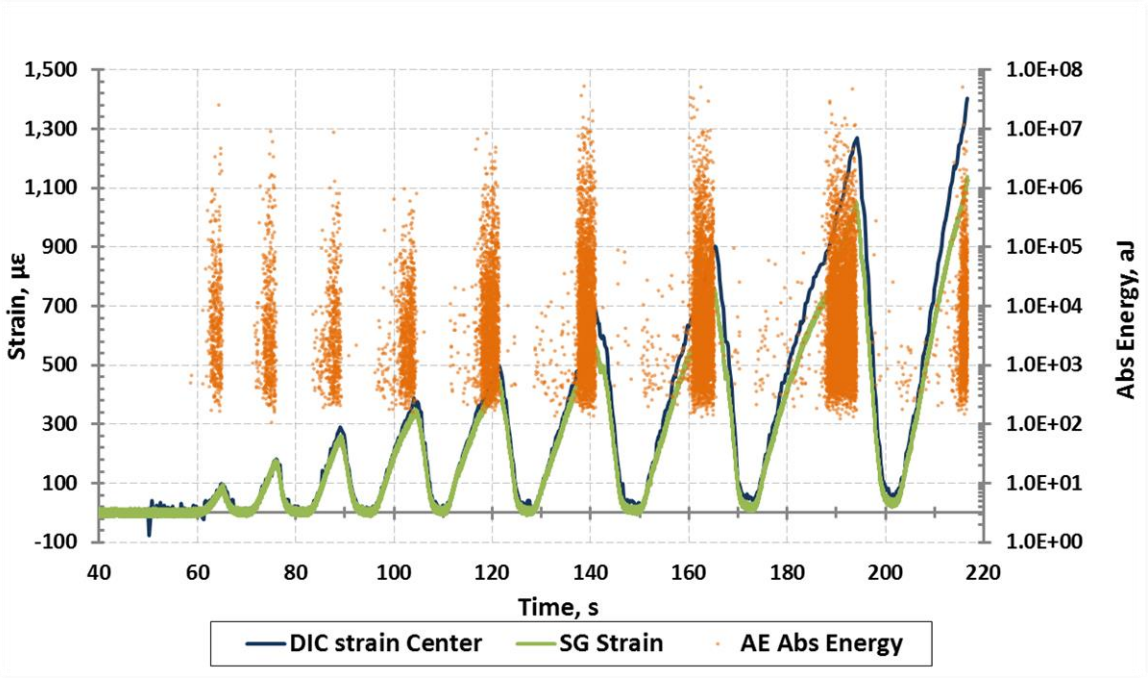

Figure 3.23 Strain and absolute energy for E-B-3 sample.

3.7 Unsupervised Pattern Recognition

Unsupervised Pattern Recognition analysis was carried out using AE data set collected from pressure cycling a relatively weak SiC_f-SiC_m sample tested in open-end burst configuration. The rupture stress, PLS stress, and PLS strain for this sample were found at 110 MPa, 46 MPa, and 250 με, respectively. The PLS strain were measured by strain gauges. Just like the previous SiC_f-SiC_m samples, it was fabricated by GA. For the clustering analysis, the AE data combined with the stress, strain, and pressure data was loaded to NOESIS software (from Mistras Group). It was noticed that in many cases the waveform were not properly detected due to precursors or several waves happening simultaneously, such as the waveforms shown in Figure 3.24. To address this problem, the waveforms were reanalyzed with a higher threshold of 62 dB. This action was perceived to be valid since nearly all individual waveforms were much shorter than the

waveform recording window of 614 μs. The data was automatically preprocessed by the software choosing 20 descriptive features for the clustering. After the preprocessing of the data, all AE events, which were normalized between 0 and 1, were placed in a multi-dimensional space based on number of descriptive features (20 in this study). Many clustering algorithms require a user input with regards to the cluster center location in that space. Because of the difficultly to properly estimate these values, K-means algorithm was chosen for this analysis because it required least amount of user input.

K-means algorithm, however, requires a manual selection on the number of clusters to be found. For the analysis, the algorithm was applied to the data for the number of clusters ranging from 2 to 10. Performance indices, Wilk's, and Rij, were minimized and the Tou index was maximized to aid in the determination of a proper number of clusters. The resulting normalized performance indices are shown in Figure 3.25. However, indices often contradicted each other. For example, if two clusters were to be chosen, Tou index value supports such selection as it is significantly higher than for other numbers of clusters. Contrary, Wilk's index is also high which indicates a bad cluster grouping. Rij, in this case, shows little change from the cluster number, therefore it was not considered for the final selection. Four clusters were chosen for this study as it showed the best tradeoff between a relatively low Wilk's index and a relatively high Tou. Ten clusters was also a viable option, however, for the initial analysis, four classes allowed a broader classification

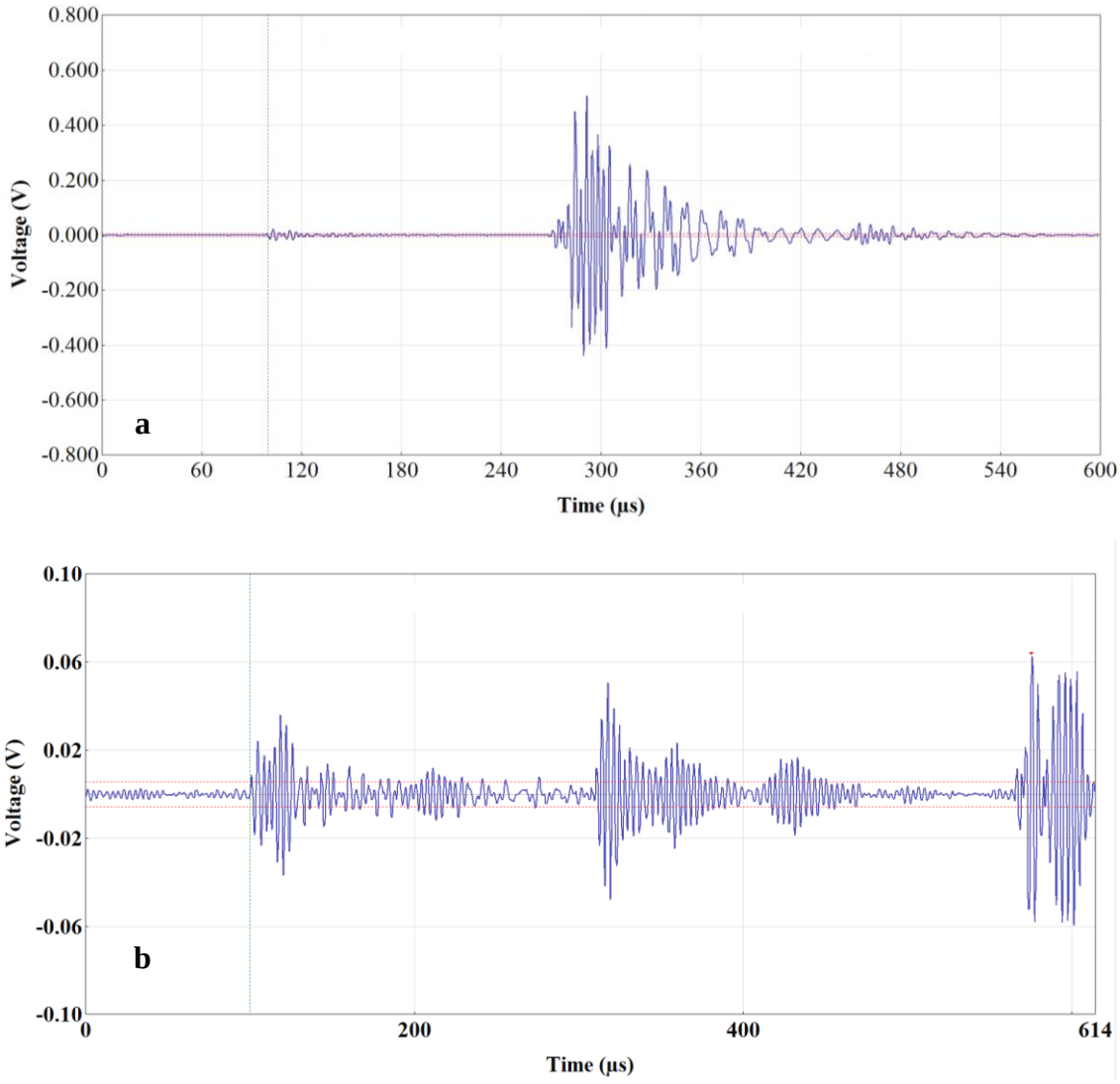

Figure 3.24 Badly detected AE waveforms: (a) a precursor had triggered the waveform recording, (b) several waves recorded simultaneously.

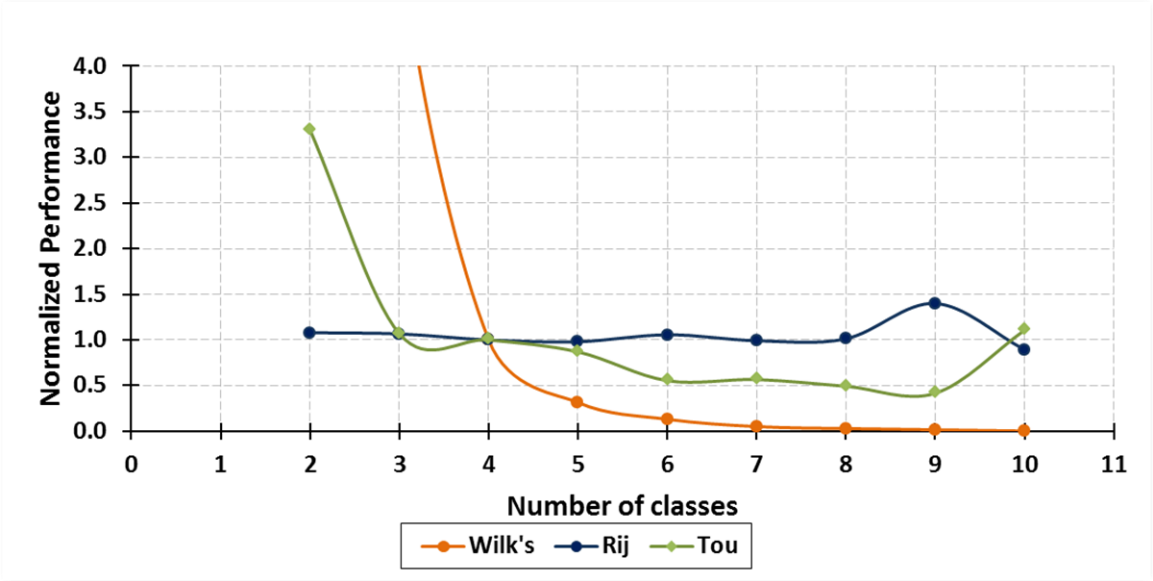

Figure 3.25 Normalized clustering performance indices plot.

To facilitate assigning UPR identified classes to mechanical damage mechanisms, several aspects had been considered. First of all, AE intensity, in a form of amplitude, and AE activity, in a form of number of AE events, had been plotted against the time separately for each of the clusters, Figures 3.26 and 3.27. From the intensity plot, it is clear to see that cluster 2 overall has the highest energy level, while cluster 1 has the least amount of energy. The other two clusters have a wide range of emitted energies. In the activity plot, it is important to note the number of events produced by each of the classes during each of the loadings. The activity for all classes becomes significant after 150 seconds, which was at 88% of PLS. Events for each of the clusters are plotted on stress-strain curve and shown in Figure 3.28.

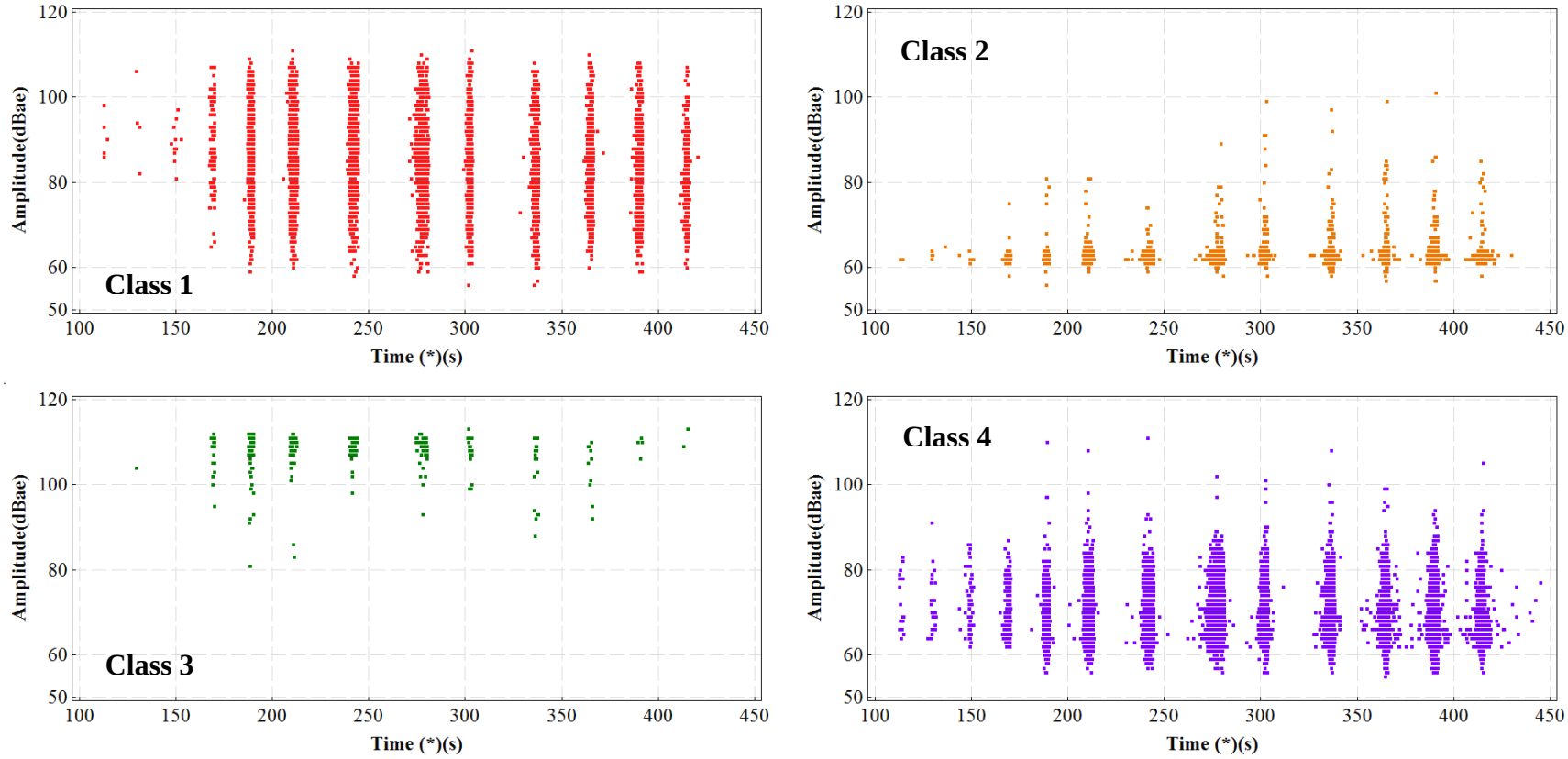

Figure 3.26 AE intensity versus time.

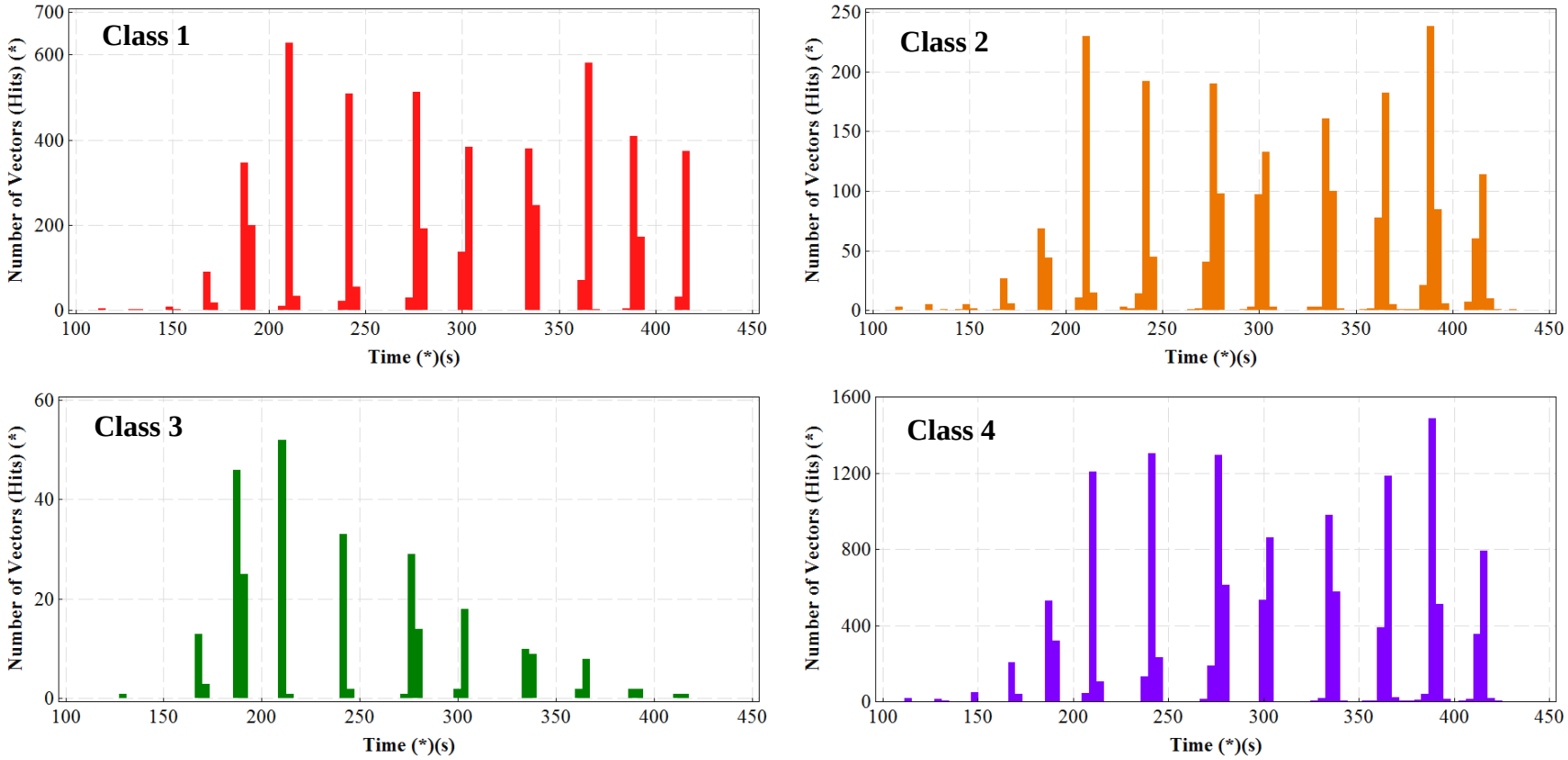

Figure 3.27 AE activity versus time.

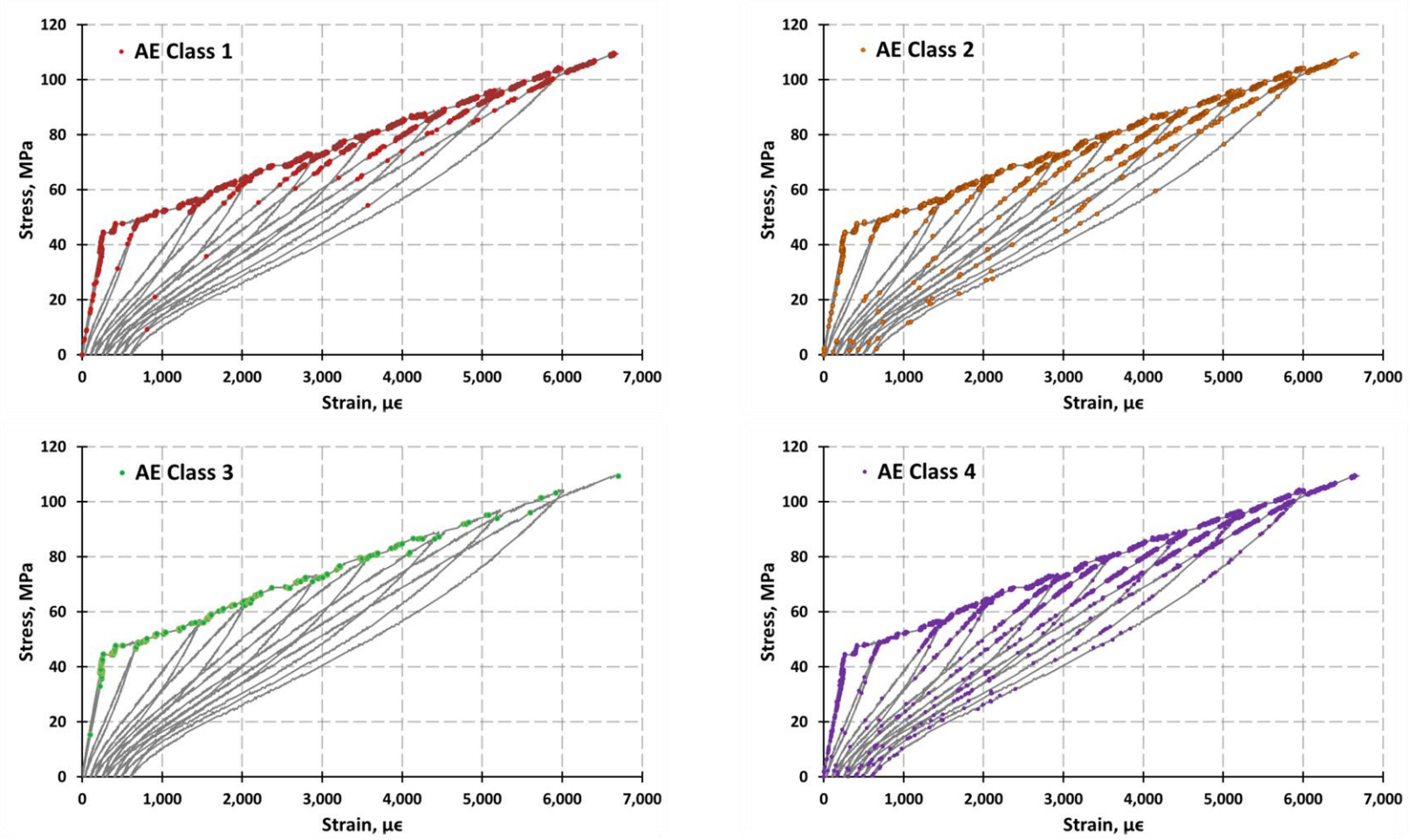

Figure 3.28 AE clusters on stress-strain curve.

From the above information the following observations were made. First of all, cluster 4, in purple, was the most active during unloading. For that reason it was assumed that the cluster 4 events were associated with frictional signals. This would explain the highest number of events during each loading-unloading cycle as each fiber-matrix interface might produce several AE events due to rubbing. Katoh showed a SEM image of the rough surface of Tyranno fiber [37] which supports the possibility of numerous frictional events.

Cluster 3 events have the highest amplitude and the longest duration as seen in Figure 3.26 and Table 3.2. Because the samples are fabricated from the III Generation of Tyranno fibers [34], these fibers are strong and dense [37] and therefore they would be expected to fail in an energetic way. For that reason cluster 3 events are attributed to the fiber breakage. However, it could be argued that near composite failure, the load is primarily supported by the fibers, and the cluster 3 activity continuously decreased with increased stress level. It is suspected that the increasing number of matrix cracks and fiber-matrix debonding increases attenuation which reduces the amplitude of a given AE signal. This behavior could be seen in Figure 3.19 and has been observed by Morscher [26]. Consequently, at the increased damage state when attenuation is higher, the fiber breakage signals would be recorded with lower amplitudes. Because of the change in amplitude and relative properties, these signals would be placed into a different cluster.

Cluster 1has largely varying amplitude signals, but it is overall much higher than the remaining cluster 2, and it has the second highest activity level. As seen in Table 3.2, clusters 1 and 3 share similar averaged peak frequency, and larger than the other two classes (2 and 4) counts to peak and counts. This suggests that the two clusters share a lot

of similarities. Since the matrix and fibers are made out of the same material, they would be expected to have similar parameters during breakage. Therefore, the cluster 1 was attributed to matrix cracking. It is also probable that the fiber breakage with lower amplitudes had been placed in this cluster. From the stress-strain curve for cluster 1, Figure 3.28, the cluster was very active during loading periods.

Table 3.2 Cluster statistics showing average values for the AE parameters and ranges of the values in the pharenthesis.

Class	Peak Counts	Counts	Frequency Centroid, kHz	Absolute Energy, aJ	Peak Frequency, kHz
1	9 (1-522)	36 (3-706)	273 (158-547)	1.6e6 (488-8.8e7)	250 (83-317)
2	3 (1-146)	7 (3-186)	340 (245-564)	1.1e4 (187-6.1e6)	270 (83-327)
3	40 (1-7422)	145 (21-9282)	307 (210-439)	7.0e7 (1.1e5-1.0e9)	251 (87-307)
4	4 (1-1320)	12 (3-2687)	311 (225-491)	3.5e4 (148-8.4e7)	273 (83-341)

The remaining cluster 2 has primarily low energy signals with a moderate activity level. These events could be attributed to alternate damage mechanisms, such as crack propagation and fiber matrix debonding. During such damage events, a crack tip travels along a path of least resistance, therefore, the amount of energy required to propagate the crack (or energy released during such events) is lower, which was consistent with the low amplitude AE events observed in cluster 2.

From the above analysis 4 classes had been attributed to specific damage mechanisms: (1) matrix cracks and fiber breaks, (2) crack propagation and fiber-matrix debonding, (3) fiber breakage, and (4) fiber-matrix friction. After these clusters are put

in duration vs amplitude graph, Figure 3.29, some correlations could be seen when comparing current results with the graph provided by Mistras for a polymer matrix composite in Figure 1.5. The fiber breakage AE signals are high energy and long duration. Mechanical rubbing is similar to the fiber-matrix friction, and the matrix cracking takes up the space in between. It is also interesting to note that this independent study produced a class that contains matrix cracking and fiber breakage together, as did the one of the classes produced by Maillet [3]. Nozawa [20] had suggested that matrix cracking might have a peak frequency of 260 kHz while our study clustered matrix cracking with an average peak frequency of 250 kHz.

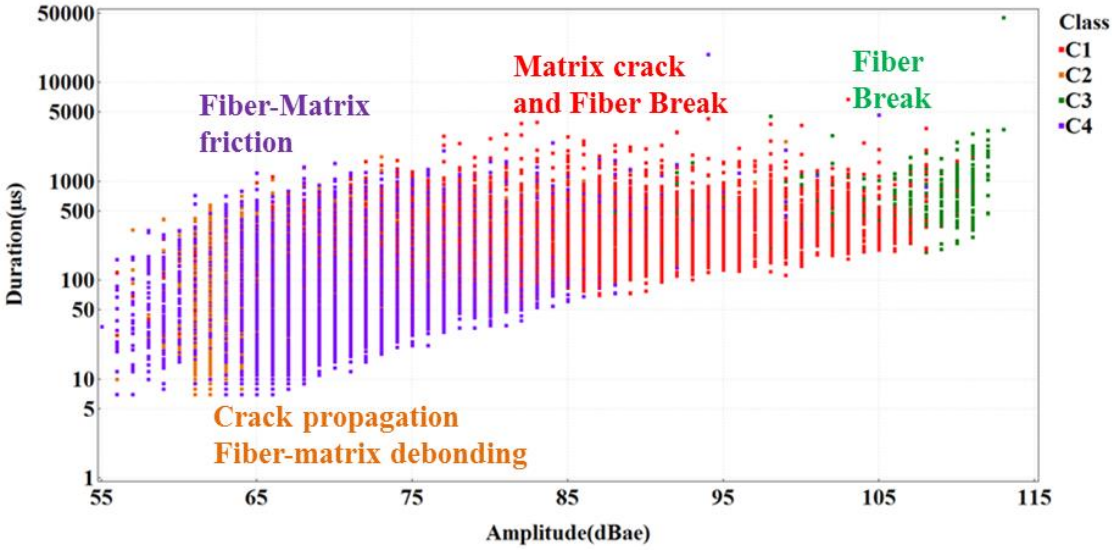

Figure 3.29 Map of all clusters on duration vs amplitude plot.

To conclude, UPR analysis produced 4 classes that were attributed to: (1) fiber break, (2) fiber break and matrix crack, (3) fiber-matrix friction and (4) crack propagation and fiber matrix debonding. The method, however, also exposed the lack of robust methodologies needed during certain steps of the analysis. Determining discriminant AE

parameters and the number of classes are facilitated but are still influenced by human subjective interpretations. Nevertheless, this independent study showed consistency with other works. Further research is needed to improve methodology of the procedure and the confidence in the analysis.

CHAPTER 4. CONCLUSIONS

In the first part of this work, two novel methods of mechanical characterization of nuclear fuel claddings had been developed and validated. The open-end burst rig has been validated with a shorter, 28 mm long, and a longer, 304 mm long, aluminum samples pressurized to 62 MPa. Strain values measured along the axis for the long sample and around the circumference of the short sample agreed to within 5% of the calculated values in the pressure range of interest. The one-end closed pressure rig was validated with a polycarbonate surrogate material. Strain maps were obtained near the plugged end using a DIC system. The resulting strain values matched well with the FE model simulation results. Therefore, it is believed that the open-end burst and the closed-end burst rigs create a uniform hydrostatic pressure in the sample under test. In particular, the closed-end test closely imitates internal pressure present in the fuel cladding during operation.

Using a photoelasticity technique and a transparent surrogate sample, the interaction between the bladder and the sample was visualized. For a short sample, a near full surface contract between the bladder and the sample was observed around 4.1 MPa. Isochromatic fringes of the photoelasticity test qualitatively showed a stress relief profile near sample edges. This profile agreed well with previously derived analytical solution. The lip study was conducted to qualitatively validate these profiles through

experimental measurements and FE simulations. The hoop stress levels off at 0.4 times of the sample's OD away from the lip.

Bladder compressibility effects had been analyzed. The closed-form mathematical solution showed that the amount of pressure received by the sample on the inside surface depends on Poisson's ratio of the polymer and the bladder tube dimensions. Experimental results from the burst rig validation tests showed negligible effects from the bladder on the pressure transmission.

Nuclear grade SiC_f-SiC_m composites of two fiber architectures were tested using the above methods. All samples showed similar properties at PLS, however, A type of samples showed significantly higher rupture pressures averaging at 99.8±5.6 MPa and greater deformations averaging at 7,626±1071 με. For samples B no visible fiber pullout indicated a strong fiber-matrix interphase which reduced the toughness of these composites. In type A samples, it was observed that both burst test methods produce equivalent results meaning that the hoop stresses are dominant in the sample failures. Using DIC strain measurements, local strain peaks were found to be significantly higher than the average strain values, ranging between 115% and 185%. The soft polymer bladder conformed well to the rough internal surfaces of these SiC_f-SiC_m composites providing a uniform pressure distribution.

Samples of A type showed strong and tough behavior capable to withstand over 8 times greater pressures than currently used Zircaloy claddings. Due to the inherent ceramic material properties, SiC_f-SiC_m cladding tubes retain their strength in high temperature environments experienced during LOCA. However, in an unlikely event that

the SiC_f-SiC_m cladding does rupture, it is expected to retain most of its shape providing the coolable geometry for the fuel pellets.

Acoustic emission data provided additional information on damage progression behavior. A good correlation had been established between PLS and the most energetic AE signals. The frequency content of AE signals generated by lead break tests showed no deviations when passed through the damaged composite material compared to signals passed through the undamaged state. AE activity for A type composite cladding samples showed deviation from commonly observed Kaiser and Felicity effects. During unloading of these composites a burst of AE signals was emitted. After reviewing other works on CMC, it is believed that the abnormal AE bursts are associated with matrix cracks closing up and forcing the contact of mismatched crack surfaces. As the final step in the AE analysis, unsupervised pattern recognition had been applied to a SiC_f-SiC_m sample producing four clusters. Through careful observations and co-examination with stress data, the four clusters were attributed to: fiber breakage, matrix cracking and fiber breakage, to friction between fibers and matrix, and to crack propagation and fiber-matrix debonding. To make more definitive source determination, more controlled tests are needed. Nonetheless, such analysis provides a stepping stone in further understanding of the progressive damage behavior of ceramic matrix composites.

REFERENCES

[1] Khalifa H.E., Deck C.P., Gutierrez O., Jacobsen G.M., Back C.A, "Fabrication and characterization of joined silicon carbide cylindrical components for nuclear applications", Journal of Nuclear Materials, (2015) 227–240.

[2] Katoh Y., Snead L.L., Henager Jr. C.H., Hasegawa A., Kohyama A., Riccardi B., Hegeman H., "Current status and critical issues for development of SiC composites for fusion applications", Journal of Nuclear Materials, (2007) 367-370.

[3] Maillet E., Godin N., R'Mili M., Reynaud P., Fantozzi G., Lamon J., "Damage monitoring and identification in SiC/SiC minicomposites using combined acousto-ultrasonics and acoustic emission", Composites Part A: Applied Science and Manufacturing, (2014) 8-15.

[4] Rohmer E., Martin E., Lorrette C., "Mechanical properties of SiC/SiC braided tubes for fuel cladding", Journal of Nuclear Materials, (2014) 6-21.

[5] Byun, T.S., Lara-Cursio, E., Lowden, R.A., Snead, L.L., Katoh, Y., "Miniaturized Fracture Stress Tests for Thin-Walled Tubular SiC specimens", Journal of Nuclear Materials, (2007) 367-370.

[6] Bernachy-Barbe F., Gélébart L., Sauder C., "Anisotropic damage behavior of SiC/SiC composite tubes: Multiaxial testing and damage characterization", Composites: Part A, (2015) 281-288.

[7] Jacobsen G., Stone J.D., Khalifa H.E., Deck C.P., Back C.A., "Investigation of the C-ring test for measuring hoop tensile strength of nuclear grade ceramic composites", Journal of Nuclear Materials, (2014) 125-132.

[8] Naslain R., "Design, preparation and properties of non-oxide CMCs for application in engines and nuclear reactors: an overview", Composites Science and Technology, (2004) 155-170.

[9] Vagaggini E., Domergue J., Evans A, "Relationships between Hysteresis Measurements and the Constituent Properties of Ceramic Matrix Composites: I, Theory", Journal of the American Ceramic Society, (1995) 2709-2720.

[10] Katoh Y., Snead L.L., Cheng T., “Radiation-tolerant joining technologies for silicon carbide ceramics and composites”, Journal of Nuclear Materials, (2014) 497-511.

[11] Rajua K., Yua H., Parkb J., Yoona D., “Fabrication of SiCf/SiC composites by alternating current electrophoretic deposition (AC–EPD) and hot pressing”, Journal of the European Ceramic Society, (2015) 503-511.

[12] Mosley K., “The stressing for test purposes of materials in tubular form using elastomeric inserts – experimental and theoretical development”, Proceedings of the Institution of Mechanical Engineers, (1982) 123-139.

[13] ASTM C1819-15, ASTM International, West Conshohocken, 2015.

[14] Ross, D.F. Jr., Hendrich, W.R., “Strength Testing Of Monolithic And Duplex Silicon Carbide Cylinders In Support Of Use As Nuclear Fuel Cladding”, Ceramic Engineering And Science Proceedings, (2006) 117-125.

[15] Nilsson K-F., Martin O., Mendes J., “The segmented expanding cone-mandrel test revisited as material characterization and component test for fuel claddings”, Nuclear Engineering and Design, (2011) 445-458.

[16] Cain, J., Case, S., Lesko, J., “Testing Of Hygrothermally Aged E-Glass/Epoxy Cylindrical Laminates Using A Novel Fixture For Simulating Internal Pressure”, Journal Of Composites For Construction, (2009) 325-33.

[17] Cohen, D., Toombers, Y.T., Johnson, A.K., Hansen, M.F., “Pressurized Ring Test for Composite Pressure Vessel Hoop Strength and Stiffness Evaluation”, American Society for Testing and Materials, (1995) 331-340.

[18] Brown, C.U., Kish III, V.L., Vanscoy II, W.M., Norman, T.L., Blaha, J.D., “Device For Applying Internal Pressure To Cylindrical Specimens”, Experimental Techniques, (2000) 19-21.

[19] Ferraris M., Salvo M., Kohyama A., “Glass-ceramic joining and coating of SiC/SiC for fusion applications”, Journal of Nuclear Materials, (1998) 1546-1550.

[20] Nozawa T., Ozawa K., Tanigawa H., “Re-defining failure envelopes for silicon carbide composites based ondamage process analysis by acoustic emission”, Fusion Engineering and Design, (2013) 2543-2546.

[21] Jung H., Hinoki T., Katoh Y., Kohyama A., “Development of a shear strength test method for NITE–SiC joining material”, Journal of Nuclear Materials, (2011), 383-386.

[22] Nozawaa T., Ozawaa K., Choib Y., Kohyamac A., Tanigawaa H., “Determination and prediction of axial/off-axial mechanical properties of SiC/SiC composites”, Fusion Engineering and Design, (2012) 803-807.

[23] Alva L.H., Huang X., Jacobsen G.M., Back C.A., “High pressure burst testing of SiCf-SiCm composite nuclear fuel cladding”, Conference Proceedings Of The Society For Experimental Mechanics Series, (2014) 387-393.

[24] Sutton M.A., Orteu J.J., Schreider H.W., “Image correlation for shape, motion and deformation measurements”, Springer, 2009.

[25] Rajan, V. P., Rossol M. N., Zok F. W,. "Optimization of digital image correlation for high-resolution strain mapping of ceramic composites." Experimental Mechanics, (2012) 1407-1421.

[26] Morscher G., Gyekenyesi A., “The velocity and attenuation of acoustic emission waves in SiC/SiC composites loaded in tension”, Composites Science and Technology, (2002), 1171-1180.

[27] Moevus M., Rouby D., Godin N., R’Mili M., Reynaud P., Fantozzi G., Farizy G., “Analysis of damage mechanisms and associated acoustic emission in two SiC/[Si–B–C] composites exhibiting different tensile behaviors. Part I: Damage patterns and acoustic emission activity”, Composites Science and Technology, (2008) 1250-1257.

[28] Moevus M., Rouby D., Godin N., R’Mili M., Reynaud P., Fantozzi G., Farizy G., “Analysis of damage mechanisms and associated acoustic emission in two SiC/[Si–B–C] composites exhibiting different tensile behaviors. Part II: Unsupervised acoustic emission data clustering”, Composites Science and Technology, (2008) 1258-1265.

[29] Momon S., Godin N., Reynaud P., R’Mili M., Fantozzi G., “Unsupervised and supervised classification of AE data collected during fatigue test on CMC at high temperature”, Composites: Part A, (2012), 254-260.

[30] Physical Acoustics Corporation, PCI-2 Based AE System Manual, 2007.

[31] Ono K., Gallego A., “Research and Applications of AE on Advanced Composites”, 30th European Conference on Acoustic Emission Testing & 7th International Conference on Acoustic Emission, 2012.

[32] Aggelis D, Barkoula N., Matikas T., Paipetis A., “Acoustic Emission as a Tool for Damage Identification and Characterization in Glass Reinforced Cross Ply Laminates”, Applied Composite Materials, (2013), 489-503.

[33] Anastassopoulos A.A, Kouroussis D.A., Nikolaidis V.N., “Structural integrity evaluation of wind turbine blades using pattern recognition analysis on acoustic emission data”, 25th European Conference on Acoustic Emission Testing, 2002.

[34] Deck C.P., Khalifa H.E., Sammuli B., Hilsabeck T., Back C.A., “Fabrication of SiC/SiC composites for fuel cladding in advanced reactor designs”, Progress in Nuclear Energy, (2012) 38-45.

[35] Heydemann, P. "On the minimum of Poisson's ratio in polymers." Kolloid-Zeitschrift und Zeitschrift für Polymere, (1963): 12-15.

[36] Nuclear Energy Agency, ”Nuclear Fuel Behaviour In Loss-Of-Coolant Accident (LOCA) Conditions”, www.oecd.org, 2009, Web. 15 Apr. 2016.

[37] Katoh Y., Ozawa K., Shih C., Nozawa T., Shinavski R.J., Hasegawa A., Snead L.L., “Continuous SiC fiber, CVI SiC matrix composites for nuclear applications: Properties and irradiation effects”, Journal of Nuclear Materials, (2013) 448-476.

APPENDIX A – INTERNAL BLADDER BURST TEST OPERATION PROCEDURE

A. 1 Purpose

Internal Bladder Burst Test system was developed to load tubular samples by means of internal hydraulic oil pressurization. The system could be used with DIC and AE acquisition systems for a mechanical characterization. The system can be set to work with one or two open-end specimens. The detailed instructions on the test procedure and useful practical tips are provided in this document.

A. 2 Safety and Training

All new personal has to be trained to perform tests on this system to avoid damage to the equipment, and personal injuries. Everybody in the close proximity to the test fixture should wear eye protection. The main source of danger is the high speed projectile particles of a failed specimen. Other minor sources of injury may arise from improper operation.

A. 3 Major Equipment and Components

1. Manually operated 207 MPa hydraulic piston cylinder,
2. Custom design burst rig,
3. Pressure transducer,
4. Analog pressure gauge.

A. 4 Procedure

A. 4. 1 General

1. Inspect the system for damage, loose connections, oil leaks, or other abnormal conditions. If a problem is detected, corrective actions must be taken before operating the system.

2. A mini-adapter is used to hold the sample in place and to provide sealing for the bladder tube. Verify that a correct mini-adapter is available for a sample to be tested. If the sample goes easily over the mini-adapter's lip but without excessive "wiggle room", the mini-adapter is a correct size.

3. Prepare the sample for the test based on research needs. Such preparation often includes bonding strain gauges and/or spray painting a speckle pattern for the digital image correlation (DIC) system or making an epoxy plug for the one open end samples.

4. Record any relevant data for you test such as sample number, dimensions, test conditions, date and any additional comments regarding the test.

A. 4. 2 Open-end samples

1. Identify all of the adapters and components used for this particular test. Measure their combined length. Add a sample's length and cut the bladder hose to the resulting total length. Cut two 22 mm long bladder reinforcements.

2. Install the bladder, bladder reinforcement, the doughnut and any other adapters needed for the test. Next, install the mini-adapter and the sample. When installing the sample, make sure to avoid any loads on brittle and/or weak samples due to misalignment or the weight of the components. Install the rest of the components and the second doughnut.

3. To avoid axial forces on the sample, alignment support bars must be used. The fixture components must be supported by the alignment bars and not by the sample. After the sample is fully installed into the rig, verify that the sample can rotate around both mini-adapter lips freely; this indicates that no axial forces are applied on the sample.

4. If the DIC is used, perform DIC calibration as outlined in Appendix B.

5. If Acoustic Emission (AE) data is used an AE sensor should be installed with an appropriate amount of Vaseline. The operator should verify adequately sensor support to avoid sensor dropping or damage during the test or after the sample burst. Verify AE sensor response with a lead break. For additional references, check Appendix C for more information.

6. Before pressurizing the sample, fill the system up with the oil while bleeding air out at the purge valve. Make sure the high pressure valves are in the correct position to allow oil flow into the burst rig. While pumping oil into the system, the analog pressure gauge may register pressures of up to 2 MPa. This is mostly attributed to the fluid friction and bladder resistance and gauge inaccuracy at such low scale. But any pressures above that indicate pressurization of the system.

7. Once system is filled with oil, release any pressure. Install protective guards to prevent area contamination and to stop high speed projectiles. The protective guard can have one side opened for the DIC cameras, but it must be open away from the operator.

8. Start data acquisition and perform desired pressurization sequence.

9. Once sample failed or desired pressures are reached, release the oil pressure and stop data acquisition systems. Make a record of any relevant observations.

10. If sample had burst, collect sample pieces and clean up the area.

A. 4. 3 One open end samples

1. In order to produce a plug in the bladder tube, clean the inside wall of the tube and apply Liquid Stich™ on one end of the tube. Fill the tube to create approximately a 5 mm long Liquid Stich™ plug. Place the bladder in a vertical position so the still liquid plug is facing the floor. Allow 7 to 10 days to fully cure. The final plug should look like the one in Figure A.1.

Figure A.1 Cured bladder end plug.

2. If a sample does not have a plug installed, a high shear strength epoxy (for example 30 MPa) should be used to make the plug. Follow the container instructions for the epoxy application. Additional curing time on top of recommended time maybe be needed based on plug thickness.

3. A sample support cone should be manufactured and bonded to the sample using the high shear strength epoxy. The cone needs to fit over the sample easily. The internal surface of the cone needs to be roughened and cleaned out for the best bonding performance.

4. Identify all the adapters to be used for the test and measure their combined length including the doughnuts. Note, an adjustable adapter must be used in this

procedure. Add the sample length to the combined length of the adapters and cut that amount off from the bladder hose. Cut one 22 mm long bladder reinforcement.

5. Install the bladder, bladder reinforcement, the doughnut and any other adapters needed for the test. Next, install the mini-adapter.

6. Install a sample support bar. Install the sample into the sample support bar and slide it up until the bladder end plug contacts the plug of the sample. This is detected by feel and the buckling of the bladder. When installing the sample, make sure to avoid any loads on brittle and/or weak samples due to misalignment or weight of the burst rig components.

7. To avoid axial forces on the sample, the alignment support bar must be installed. The fixture components must be supported by the alignment bars and not the sample.

8. Make sure the high pressure valves are in the correct position to allow oil flow into the system. Before pressurizing the sample, fill the system with the oil while bleeding air out at the purge valve.

9. Since the same line is used to fill the oil up and to bleed the air out, some care should be taken during this step. To bleed the system keep the purge valve closed while applying light pressure into the system until the bladder feels firm to touch. Keep adjustable adapter in a contracted position so a section of the bladder is exposed. When pressure is applied, wiggle the bladder hose and push it away from its vertical axis. Let it sit in that condition for a minute or two. Then, while still pushing the bladder to one side, open the purge valve. Repeat this step until the bladder fills up with oil (about 3 times).

10. Once the air is blead out, reposition adjustable adapter in its operating position.

11. Install additional shaft collars to support sample support bar and preventing the assembly from sliding down.

12. Perform steps 4, 5, and 7-10 as described in two open ended samples procedure.

A. 5 Calibration and Controls

The pressure transduce requires an annual calibration. If strain gauges are used, the strain gauge factor must be recorded with the test. DIC calibration score and the average projected error must be recorded with the DIC analysis. If DIC results are recalculated, the new average projected error must be recorded. For the AE measurements, the air suspended work table should be activated to reduce chances of detecting irrelevant AE signals.

APPENDIX B – DIC CALIBRATION PROCEDURE

B. 1 Purpose

Digital Image Correlation (DIC) system requires a calibration procedure to establish special references. For a 3D system (using two cameras or more), calibration determines physical location of one camera in relation to the other. This procedure outlines steps need to calibrate the system and additional useful tips.

B. 2 Procedure

1. For the calibration procedure a reference target is needed. The target must be provided by DIC venders or printed using Target Generator software. If target is to be printed, print scale must be set to an "actual scale". The printed target must be bonded to a rigid flat surface. The settings used to generate the target must be recorder and input to Vic3D software.

2. First, set up the camera system for the test to be performed. Focus, depth of field, light intensity, uniform sample illumination, sample position in the viewing area, camera shutter speed, speckle pattern are all must be evaluated before starting the calibration.

3. For the calibration, a minimum of 15 images of the target must be taken. The target should be tilted in different directions for a best calibration. The tilt can be as large as the depth of field of both cameras allows it. For the best results, the target should be

supported in a rigid apparatus to prevent hand shaking during image taking. VicSnap is the native DIC software for the image acquisition. If another software is used, image capture must be synchronized in time to a small fraction of an exposure time.

4. Input calibration images into Vic3D program for processing. From the main menu ribbon select calibration option to bring up a calibration window as shown in Figure B.1. Select your correct target size (if not available, create from the target setting obtained in step 1). If the sample shape is complicated, set distortion order to a higher value. If shape is simple, value of 1 is a default choice and could be used. Click analyze button.

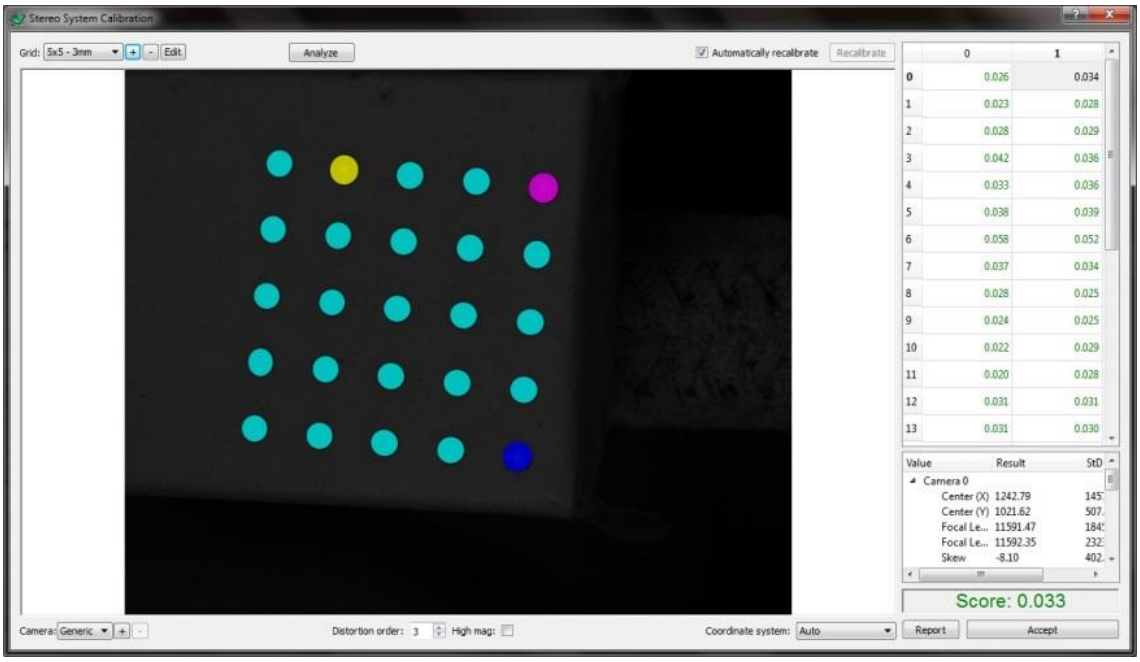

Figure B.1 DIC calibration window with a good score.

5. Note the calibration score. Default acceptable margin is 0.1 with lower values meaning better calibration (also shown in green color). If the score is too high, check image quality for an out of focus areas, light intensity variations, quality of the target

print, and the target position in each of the cameras viewing areas. If bad calibration is detected, repeat steps 3-5.

APPENDIX C – ACOUSTIC EMISSION SETUP

C. 1 Purpose

Acoustic emission data acquisition system needs to be setup properly in order to obtain repeatable and meaningful results between different tests for similar specimens. The settings include hardware parameters, software parameters, sensors, mounting and coupling.

C. 2 Procedure

1. Use AEWin for data acquisition. Open an AE hardware Layout file that has been created for a specific sample type.

2. Verify that the preamplifier gain in the "hardware setting" menu in the software matches the physical gain setting on the preamplifier device.

3. Perform sensor consistency test as outlined in ASTM E2075. Do not use the sensor if it fails the test.

4. Mount the AE sensor on the sample to be tested. Apply vaseline type coupling between the contact surfaces of the sensor and the sample. The sensor should be pressed against the sample for a better signal detection. Rubber bands work well in providing adequate compression forces for smaller sensors.

5. WARNING: avoid sensor dropping on hard surfaces (such as steel top table or a concrete floor). One bad drop can cause a total sensor loss. Smaller sensors, such as

Nano30, can be supported by their wires taped to the rig. A custom-made silicon cover provides additional protection which should be used at all time if possible.

6. Once AE sensor is mounted onto the sample, a lead break test should be done on the sample's surface. If the sensor measurement is close to the expected amplitude value after accounting for the attenuation, the sensor has a good contact with the sample. If the signal is significantly weaker or no signal is detected, mounting should be checked.